Department of Physics and Astronomy
Heidelberg University

Bachelor Thesis in Physics
submitted by

Elias Bürkle

born in Marburg (Germany)

2022

Thickness determination of free-standing liquid crystal films via autocorrelation measurements

This Bachelor Thesis has been carried out by Elias Bürkle at the
Max Planck Institute for Nuclear Physics in Heidelberg
under the supervision of
Dr. Laura Cattaneo

Acknowledgement

I would like to express my gratitude towards Dr. Laura Cattaneo, for her guidance and great personal and professional support throughout this thesis. Also, I want to thank Prof. Dr. Thomas Pfeifer for reviewing my work on behalf of the university Heidelberg. I especially thank Patrick Friebel for his introduction to the laser laboratory and constant assistance with my experimental setup. Without him, this thesis would not have been possible. I cordially thank Michael Weiß Mare from the MPIK electronics department, for providing and maintaining the LC holder software. My thanks also go to Yannick Steinhauser from the MPIK precision engineering department, for the design and improvements of the LC holder. I am further grateful to the MPIK construction department under the supervision of Frank Müller for the fast machining of parts needed for my setup.

Abstract

0.1. English

The goal of the bachelor thesis presented is to determine the thickness of mechanically formed free-standing liquid crystal films, presenting smectic and nematic phase, using an intensity autocorrelator. The thickness has been measured as a function of two specific parameters, temperature in the range of $22°C$ to $35°C$, thus impacting on the LC phase, and formation speed. A correlation of liquid crystal film thickness and temperature was found. In this process, a dynamic modification of alignment of the free-standing liquid crystal film with respect to time, dependent on temperature and formation speed, was observed and preliminary results are presented here.

0.2. German

Ziel der hier vorgestellten Bachelorarbeit ist es, die Dicke von mechanisch gebildeten freistehenden Flüssigkristallfilmen in smektischer und nematischer Phase mit Hilfe eines Intensitätsautokorrelators zu bestimmen. Die Dicken wurden in Abhängigkeit von zwei spezifischen Parametern gemessen: Temperatur im Bereich von $22°C$ bis $35°C$, die sich auf die LC-Phase auswirkt, und Bildungsgeschwindigkeit. Es wurde eine Korrelation zwischen der Dicke des Flüssigkristallfilms und der Temperatur festgestellt. Bei diesem Prozess wurde eine dynamische Änderung der Ausrichtung des freistehenden Flüssigkristallfilms in Abhängigkeit von der Temperatur und der Bildungsgeschwindigkeit beobachtet, und die vorläufigen Ergebnisse werden hier vorgestellt.

Table of Contents

1. Introduction

The ultra-fast liquid crystal dynamic (ULCD) group at the Max-Plank-Institute für Kernphysik Heidelberg (MPIK), studies the dynamics of liquid crystals (LC) from the picosecond down to the attosecond timescale. Changes of the LC refractive index induced by the interaction with an intense laser pulse leads to the subsequent relaxation via molecular vibrations and in the THz spectral range. To observe this, there is a need for high quality LC samples with precise orientation and dimensions. Thin free-standing and temperature-controlled LC films provide a suitable solution which allows the direct investigation of the sample with the desired radiation avoiding substrates.
The ULCD group, in collaboration with the mechanical and electronic workshop at the MPIK, developed a motorized holder to generate such free-standing films. Previous studies of such devices suggest the possibility of varying the LC film thickness of these samples by controlling temperature, volume and operating speed. Typically, the LC free-standing films have a thickness of about $1\mu m$, and measurement at this scale requires a high-precision setup. By exploiting the stretching of the optical path, it is possible to achieve the required accuracy using an intensity autocorrelator. This thesis addresses the systematic characterization of such free-standing LC films in terms of thickness and its dependencies on different parameters in order to be able to achieve the desired degree of control.

2. Background

2.1. Liquid Crystal

2.1.1. States of Matter

Liquid crystals (LCs) are materials that experience an aggregation state with both, fluid and crystalline features. There are three kinds of LCs. They can be divided between lyotropic, metallotropic and thermotropic. The work presented concentrates on the thermotropic LCs, in which the state of matter depends mainly on temperature. Such molecules are called mesogens. We will refer to them as LCs in the future. Opposed to other materials, LCs exhibit at least two phase transitions between the fluid and crystalline state. Typically, with rising temperature, there is a smectic phase after the crystalline phase, followed by a nematic phase, right in before the fluid state. While the isotropic state and the solid state are well known, the nematic and smectic phases need further explanation [1].

2.1.2. Nematic State

The nematic phase is characterised by a long-range order of orientation but with no long-range positional order of the molecules, which implies an aelotropic molecular shape. Similar to liquids, nematics do not have a periodic lattice or grains and a low viscosity [1]. In our experiment, we used 4-octyl-4-biphenylcarbonitrile (8CB), which is rod-shaped. To characterise the long-range orientational order, we use the director $\vec{n}$, which describes the direction in which the molecules tend to align. We cannot differentiate between the ends of the rods, therefore $\vec{n} \equiv -\vec{n}$ for our purpose. To quantify this, we introduce the orientational order parameter

$$S = \frac{1}{2}\langle 3cos^2(\beta) - 1\rangle. \tag{2.1}$$

Here β denotes the angle to $\vec{n}$ of each molecule. The angled brackets express averaging over finite space. We can ignore the angle ϕ in the plane of $\vec{n}$ due to the averaging. The order parameter describes the overall orientation of our LC, where zero is total disorder (isotropic state) and one is total order (solid state). At the phase transition isotropic-nematic it jumps discontinuously from zero to a non-zero value [1].

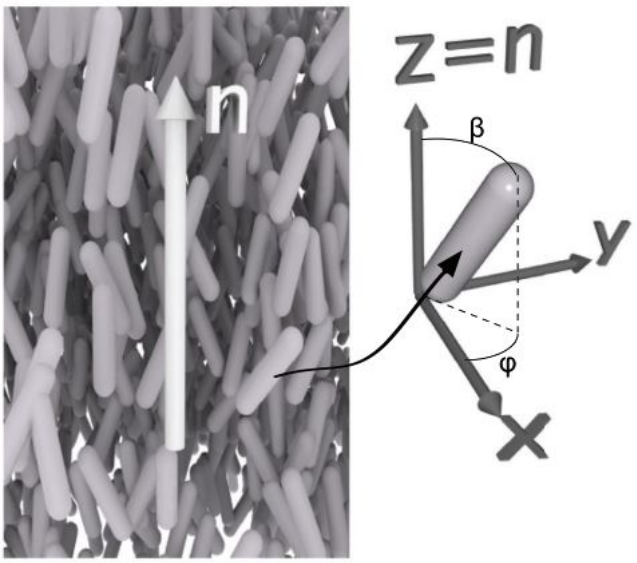

Figure 2.1.: Graphic of the nematic phase in 3D and director $\vec{n}$ of a mesogen [1].

2.1.3. Smectic State

A layering structure defines the smectic phase. This, however, should not be taken too literally. Contrary to a crystalline structure, boundaries in the smectic structure are defined by an electron density modulation along one direction in a quasi-long range. There are different smectic phases, the two most important ones are the smectic-A (SmA) phase, where the director $\vec{n}$ is indistinguishable from the layer normal vector $\vec{k}$. And the smectic-C phase (SmC), here the director is tilted with an angle θ. This results in a thinner layer structure compared to the SmA phase. The thickness of these layers and, with that, the tilting angle θ influences the free energy of this state [1]. In this experiment 4-Cyano-4'-pentylbiphenyl (8CB) was used due to its ability to form free-standing films. The phase transitions are listed in the table below.

Phase	Temperature [C°]
Crystaline	< 20.85
Smectic-A	20.85-33.55
Nematic	33.55-39.85
Isotropic	> 39.85

Table 2.1.: Phase transitions of 8CB [2].

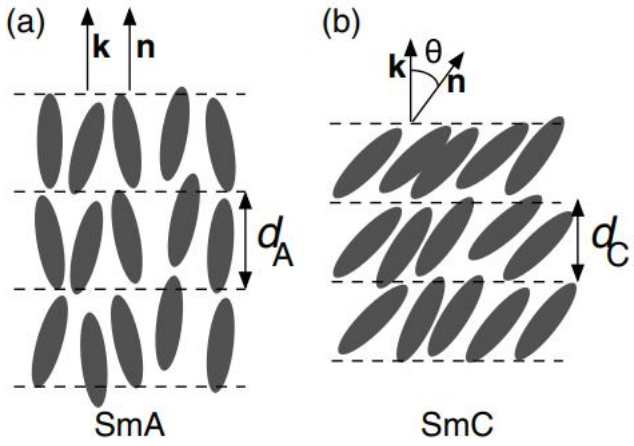

Figure 2.2.: (a): Smectic-A phase with director $\vec{n}$ along layer normal $\vec{k}$ with layer thickness d_A.
(b): Smectic-C phase with director $\vec{n}$ angled with θ to layer normal $\vec{k}$ and layer thickness d_C [1].

2.1.4. Birefringence

LCs are optically anisotropic. Due to their rod-like molecular structure, the refractive index parallel to the director $n_\parallel$ differs from the one perpendicular to the director $n_\perp$. The optical axis is $\vec{n}$. To quantify this, we define the birefringence

$$\Delta n = n_\parallel - n_\perp. \tag{2.2}$$

For most rod-like LCs $\Delta n > 0$. This is called uniaxial, and the ordinary refractive index is $n_o = n_\perp$. The extraordinary one n_e depends on the direction of light propagation with $n_e \leq n_\parallel$. The anisotropic properties also change the polarization $\vec{E}$ of light. Linear, elliptical and circular polarization can all occur, also changing the main oscillation direction and inverting the rotation handedness are possible, depending on the arrangement of the mesogens. For light travelling along the optical axis $\vec{n}$ this effect vanishes, and only $n_\perp$ is experienced, because of the transversal nature of light. A sample prepared in such a way is called homeotropic. If the sample is prepared in a way that the propagation of light is perpendicular to the optical axis $\vec{n}$, it is called planar and experiences the full birefingence Δn. In case of a non-homeotropic incidence, the beam splits into two rays, the ordinary and the extraordinary ray [1].

2.1.5. Free Suspended LC Films

Drawing LC with a wiper blade over a hole in a polished material generates, like soap, a film of LC. As samples, these LC films have a variety of advantages. Through different methods, it is possible to draw thin films with a thickness from a single layer, thus a couple of molecules up to films with thousands of molecular layers. In the smectic phase,

these films tend to be stable for days, additionally thinning forces of the surface tension drive incomplete layers and impurities out of the sample. This creates a very well-aligned and uniformly thick surface in the centre. For 8CB we expect the SmA phase in a narrow mosaic arrangement. This means the director is parallel to the surface vector, so a beam coming at normal incidence to the film only experiences the ordinary refractive index [5]. In this setup, the film is drawn by wiping a blade across a hole in a copper block. A picture of a free-standing LC film can be seen in Figure 2.3.

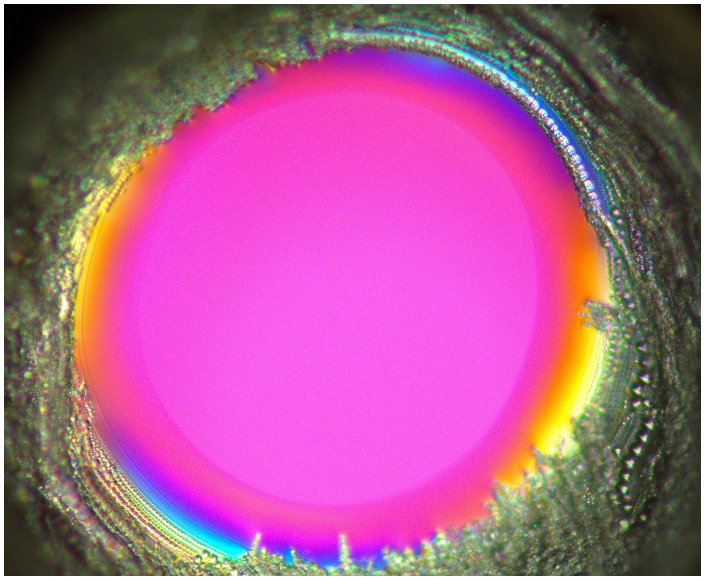

Figure 2.3.: Microscope image of a 8CB free-standing film. The uniform color in the center implies an uniform thickness and homeotropic alignment. A thin meniscus of varying thickness and alignment is visible.

2.2. Optics

2.2.1. Refraction

For non-birefringent materials and considering the ordinary ray, the light propagates according to the Snell's law.

$$\frac{\sin\phi_1}{\sin\phi_2} = \frac{n_2}{n_1}. \tag{2.3}$$

Here ϕ_1 denotes the angle of incidence to the plane vector of the sample, ϕ_2 is the resulting angle of the ray to the plane vector, n_1 the refractive index of the material before the sample and n_2 the refractive index of the sample material at a given frequency. For birefringent materials, it is more complicated. As the light beam passes through the sample, it gets split into two beams, the ordinary, which behaves according to Snell's law and the extraordinary. The extraordinary ray experiences a refractive index of n_{eff},

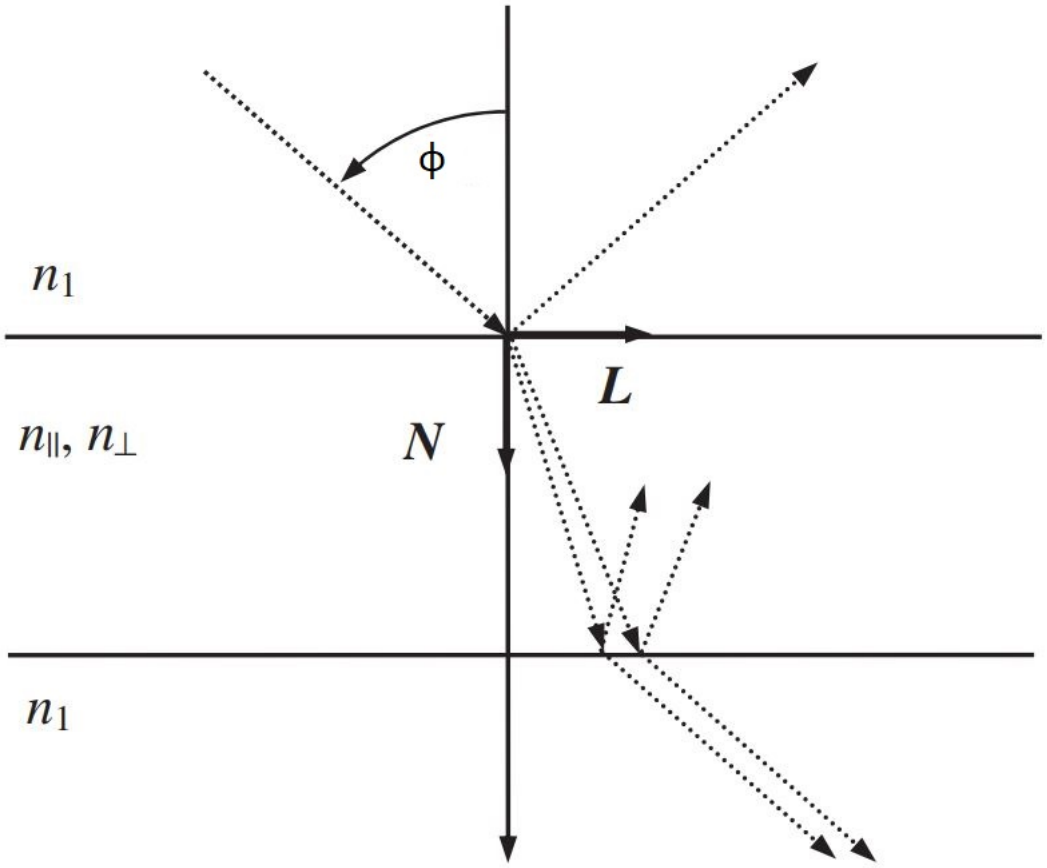

Figure 2.4.: Schematic of Snell's law for a birefingent material [13].

which is determined by the polarization and the angle amongst other factors. It lies between n_o and n_e.

2.2.2. Second Harmonic Generation (SHG)

Also known as frequency doubling, second harmonic generation is the interaction of two photons of the same frequency with a nonlinear material resulting in a new photon with double the frequency. This is a nonlinear process, which means the polarization $\vec{P}$ is not linearly proportional to the electric field $\vec{E}$ of the light. In this particular process, the energy of the resulting photon is twice the energy of the incoming photons. That means the two incoming photons of frequency ω excite the molecule to a higher state and by reverting back to the ground state, a single photon of frequency 2ω is emitted. We get from energy conservation

$$\omega_1 + \omega_1 = \omega_0, \tag{2.4}$$

here ω_1 is the frequency of the incoming and ω_0 of resulting photons. From the conservation of momentum follows

$$\vec{k_1} + \vec{k_1} = \vec{k_0}. \tag{2.5}$$

Here $\vec{k_1}$, $\vec{k_0}$ are the wave vectors respectively. For SHG these two conditions must be satisfied at the same time. Taking into account the relation

$$|\vec{k}| = \frac{n\omega}{c}, \tag{2.6}$$

c corresponds to the speed of light in vacuum. We can see this may not be true. Plugging in our frequencies, with $\omega_0 = 2\omega_1$, yields

$$n(\omega_1) = n(2\omega_1). \tag{2.7}$$

A monorefringent material cannot satisfy this due to dispersion. However, there are different methods to achieve this, in our experimental setup we use a birefringent barium borate crystal (BBO). By turning its orientation compared to the incoming beam, we can adjust the effective refractive index n_{eff}, that extraordinary ray experiences, such that

$$n_o(\omega_1) = n_e(2\omega_1). \tag{2.8}$$

This is called phase matching. Due to its negative birefringence, BBO supports type one phase matching for wavelengths $409.9nm$ to $3500nm$. Type one means the polarization of the two incoming photons is ordinary, and the resulting photon has extraordinary polarization [12].

3. Setup

3.1. LC Holder

To create free-standing LC films, the ULCD group, in cooperation with the Max Planck Institute electronics department and the precision engineering department, developed a motorized LC holder. By controlling the working parameters, a reliable and consistent sample can be created.

3.1.1. Design

The LC holder consists of a copper block, with a heating mechanism and a temperature sensor. A copper blade is clamped to a stepper motor that moves it over the holes. The upper $1mm$ hole has screw threads and is utilized as a LC deposit. By rotating a screw forward, LC is displaced and leaks out the front. The second $3mm$ hole has a $45°$ bevel on the inside and is the place where the films are created. The copper blade moves over the dispenser hole and drags LC over the sample hole a thin LC film is now standing in the $3mm$ sample hole. Below the $3mm$ hole, there is another $5mm$ hole, that can also be used for film formation.
The holder and dispenser is operated by a software written in Python, see Figures 3.2 and 3.3. The motor speed is variable, and the travelling distance can be adjusted by moving the turning points. The software monitors the temperature of the copper block and the ambient temperature. With the dispenser software the amount of LC can be controlled. There is also a function for an automated trigger, that dispenses a fixed amount of LC every time an electric signal arrives. Also, the contact pressure of the wiper blade against the copper block is adjustable.

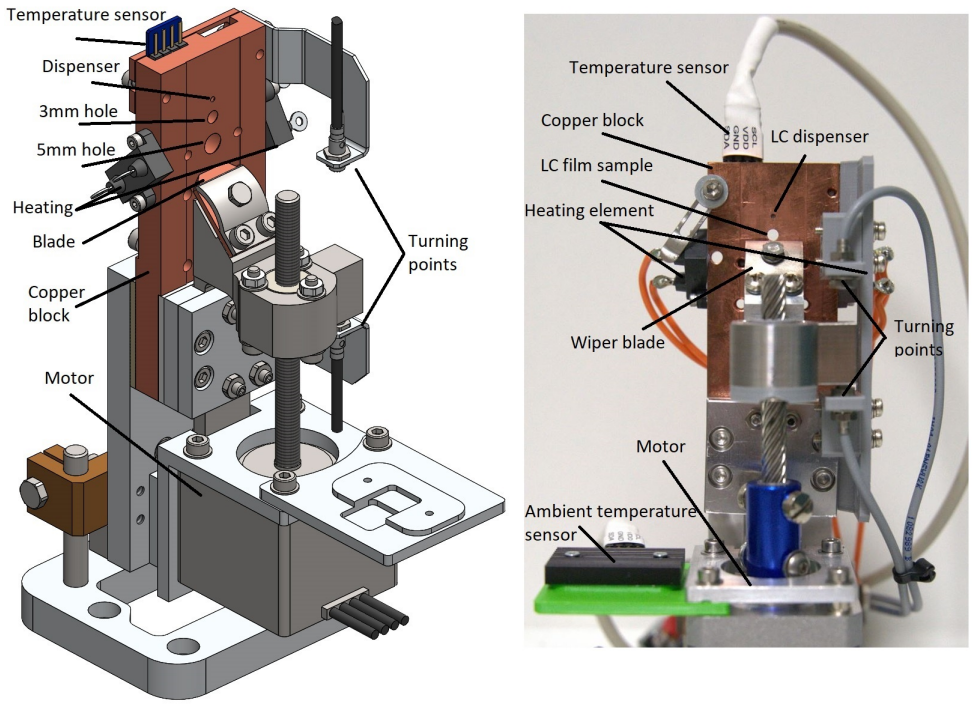

Figure 3.1.: LC holder schematic on the left and a picture of the LC holder on the right.

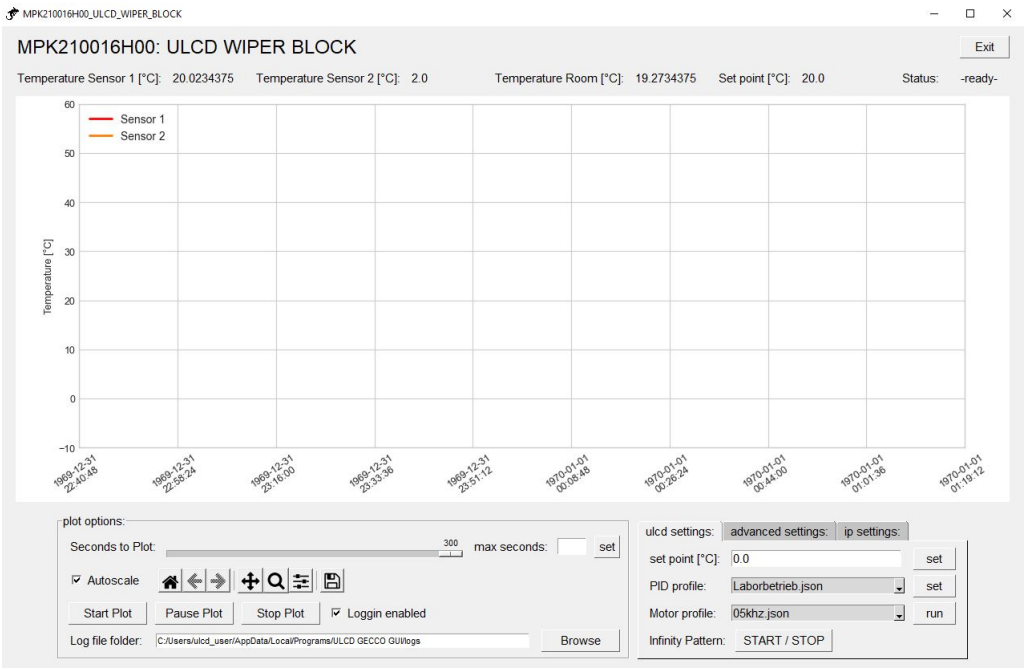

Figure 3.2.: The software that controls the holder, temperature can be set and the wiping speed is adjustable.

3.1.2. LC Film Formation

After the film is formed, the mesogen layers start to move and align themselves towards the film surface. Surface tension pulls the LC to the smallest radius. Therefore, the 45° inner bevel ensures a repeatable film position and alignment. Copper is used because of its thermal conductivity. The thickness of these films stems from many different factors, surface finish, temperature, wiping speed, amount of LC, hole diameter and pressure of the blade, to name a few. A further complication arises from the fact that these variables might not have a continuous influence on the film thickness. For instance, adding more LC would increase thickness only for a small margin. After that, an opaque meniscus forms at the edges and, depending on the volume, the film returns to normal, deforms or breaks shortly after. For thicker films, gravity can lead to a gradient alteration of the shape with more LC at the bottom, and for larger holes, the temperature gradient can cause a phase transition towards the inner regions. This results in an amphitheater-like layering with the thinnest part at the middle [8]. Temperatures outside of the smectic or nematic phase alter the properties immensely. Changing the force of the blade against the copper block can lead to no film formation, if too little. If the contact pressure is too high, the copper block and the blade can be damaged. Also, the motor can start to stutter and overheat, which further influences other variables. To stay on top of things, after finding suitable operating conditions, only wiping speed and temperature are changed. In this process, different blade designs have been tested, among them are a flat copper blade, a copper blade with a circular section removed at the top and a copper blade with a circular section added to the top, two teflon blades, one flat and one with a circular section removed. As shown in Figure 3.4, the left blade is a damaged old one because the new one is currently in use. The middle blade with the circular shape added was designed to simulate a damaged blade, but with a smooth polished surface. The repeatability and film stability amongst them have been tested. Here the flat copper blade and the copper blade with the circular indentation performed the best. The teflon blades were too soft, and therefore the point of contact was not stable enough and in the wrong place. To counteract this, an elongated clamp was designed. That improved the stability of the contact point, but the teflon blades were still outperformed by the copper ones. The flat copper blade was used in further tests, given the overall high level of performances.

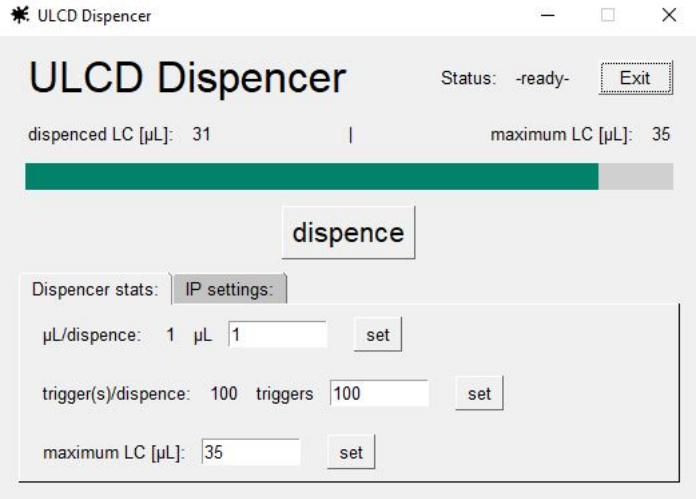

Figure 3.3.: The dispenser software, the amount of LC can be varied and a refreshment rate can be set.

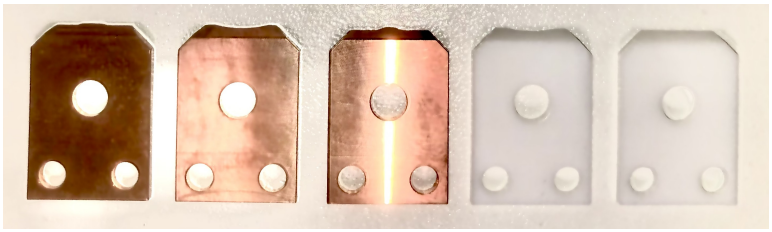

Figure 3.4.: Different wiper blades.

Next, a qualitative test of reliability in film making was performed. The temperature of the copper block was set to $29°C$. For different wiping velocities, an amount of LC was placed on the block. The number of films drawn and the success rate were then observed. At this moment, the dispenser was not yet implemented, and LC viscosity made it extremely difficult to dose the LC on the copper block accurately, so the amount of LC was estimated by a comparison to water droplets from a μl pipette. The average refill amounted to about $3\mu l$. After the film is formed, the alignment of the mesogens takes some time, depending on the temperature. This can vary between a couple of minutes up to an hour.

Blade velocity $[mm/s]$	Average number of films per refill	Success rate
5	81	0.97
10	128	0.80
40	94	0.57

Table 3.1.: Testing the operating conditions of the LC holder.

3.1.3. Operating Conditions

To ensure stable working conditions, an operating procedure needs to be followed. First, a working contact pressure and moving distance are chosen. Then these parameters are fixed and will not be changed. After the dispenser is filled, a motor moves the screw forward and squeezes about $1\mu l$ of LC out of the hole. Then the wiper is driven, with a velocity of $2.5mm/s$, over the sample hole until a film is formed. This may take a couple of tries, because the LC need to be dragged around it. After the first film formation, this is achieved and the film is popped. The holder can be used now. When no more films are forming, after ten tries, an additional $1\mu l$ is dispensed, and the operating procedure is repeated. This procedure should regulate the amount of LC on the copper block.

3.2. Thickness Measurement

The thickness measurement was performed using an intensity autocorrelator. By measuring the displacement of the optical pathway, the thickness can be calculated.

3.2.1. Autocorrelation

To measure an event in time, it is necessary to have a shorter event, like a fast photodetector. However, with ultra-short laser pulses in the femtosecond range, this is difficult because they are the shortest events available. An autocorrelator gets around that problem by using the laser pulse to probe itself. This is done by dividing the beam in two using a beam splitter. With the use of a movable mirror, the length of one of the beam

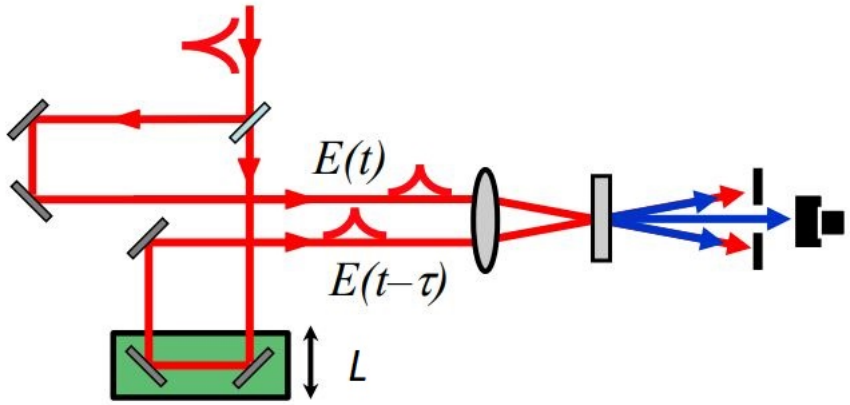

Figure 3.5.: Schematic of an intensity autocorrelator [7].

paths is changed, meaning that one of the two pulses is, delayed in time, with

$$\pm\tau = \frac{\pm 2L}{c}. \tag{3.1}$$

Here τ describes the difference in time when the pulse is arriving, L is the moving distance of the mirror, and c is the speed of light. The factor 2 takes into account, that the beam is usually travelling twice the distance, due to geometry considerations. The two rays then are both directed into a nonlinear crystal. If they overlap there in time, SHG occurs, and it can be detected by means of a photodiode as represented in Figure 3.5.
The resulting intensity can be expressed as follows

$$A(\tau) = \int_{-\infty}^{\infty} I_1(t)\, I_2(t-\tau)\, dt. \tag{3.2}$$

I_1 and I_2 are the intensities of the beams without and with the delay respectively. For this to occur, some geometric conditions must be satisfied, as seen in Figure 3.6.

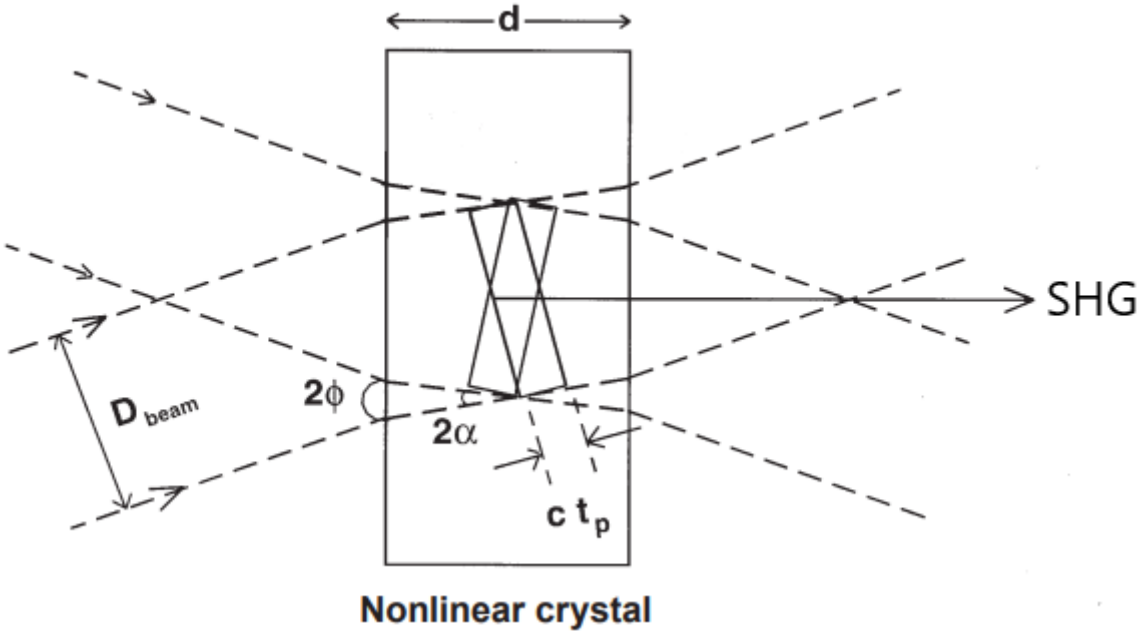

Figure 3.6.: Schematic of SHG in a nonlinear crystal [9]. D_{beam} is the beam diameter, ct_p the spatial pulse length, ϕ the angle of incidence before refraction and α after refraction.

For a non-collinear geometry, the phase matching condition from equation 2.8 becomes

$$n_o(\omega)\ \cos(\alpha) = n_e(2\omega). \tag{3.3}$$

For BBO this results in a maximum angle of incidence $\alpha = 19.23$. Figure 3.6 concludes that a complete temporal overlap is possible, if equation 3.4 is true

$$D_{beam}\ \tan(\phi) \geq ct_p. \tag{3.4}$$

Furthermore, the thickness d of the crystal must satisfy

$$d\ \cos(\phi) \geq ct_p. \tag{3.5}$$

The resulting beam is bisecting the others and its intensity depends on the delay between them, with the maximum at $\tau = 0$. Measuring the intensity for different delay positions yields an intensity autocorrelation curve, as seen in Figure 3.7. If the pulse shape is known, the pulse length can be determined from the full width half maximum (FWHM) [9]. Assuming a Gaussian shape the pulse length l_p would be

$$l_p = 0.709\, l_a, \tag{3.6}$$

Where l_a is the FWHM of the autocorrelation. Resulting in an estimated pulse length $l_p = 14.18\mu m$ or pulse duration of $t_p = 47fs$. Comparing this to the manufacturer

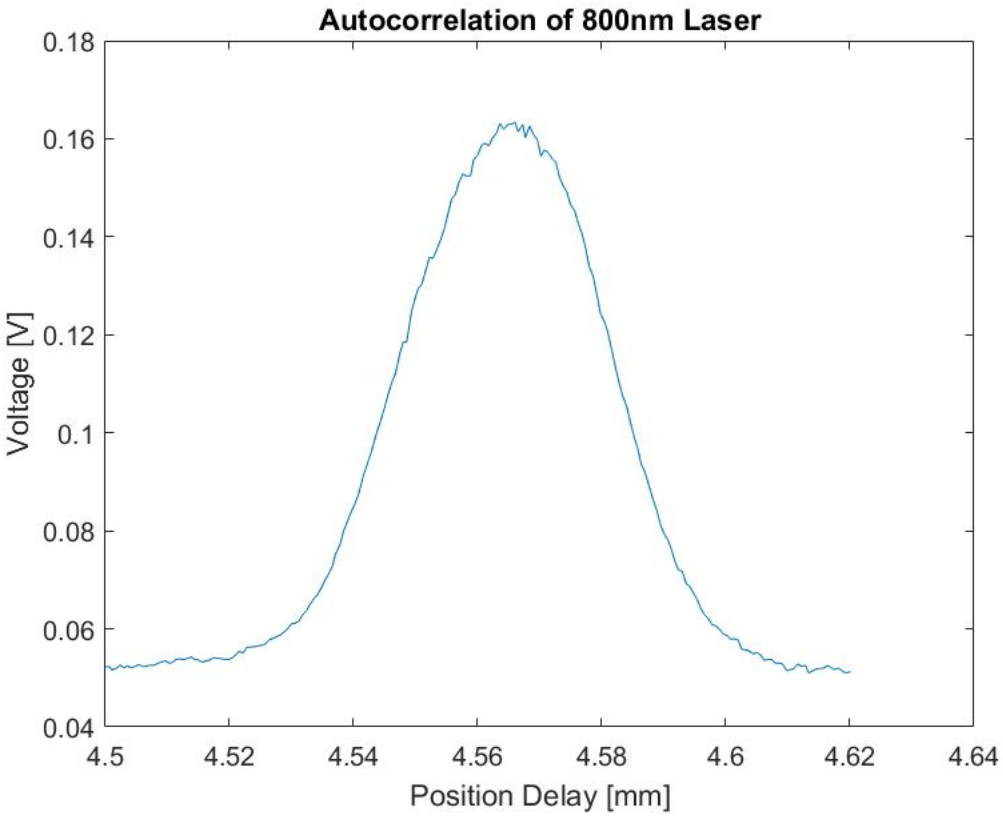

Figure 3.7.: Intensity autocorrelation.

specifications of $t_{pulse} = 35fs$, a slight discrepancy can be noted. Optical elements such as the lenses and the beamsplitter may be the cause for that. Also, mirrors alter the pulse length, but this effect is negligibly small. Using an autocorrelator to measure the thickness of a sample requires the measurement of two autocorrelation curves, one with the sample and one without to be used as a reference. The speed of light depends on the medium it travels through. This means that two light pulses travelling the same distance but in different mediums arrive at different times. To quantify that, we introduce the optical path length

$$l_o = \int_C n \, ds, \tag{3.7}$$

with n being the local refractive index, with respect to the distance s travelling along the path C. The difference of the optical path then results in

$$\Delta l_o = l_{o2} - l_{o1} = \int_{C_2} n_2 \, ds_2 - \int_{C_1} n_1 \, ds_1. \tag{3.8}$$

Since both paths are the same except for the sample, this can be simplified into

$$\Delta l_o = s_{sam} \, (n_{sam} - n_{air}), \tag{3.9}$$

with s_{sam} and n_{sam} being the sample thickness and refractive index respectively, and n_{air} the refractive index of air. If we now compare the peak position of the autocorrelation of the reference measurement p_{ref} to the peak position of the autocorrelation of the sample measurement p_{sam}, we can calculate the sample thickness as follows

$$s_{sam} = \frac{p_{ref} - p_{sam}}{n_{sam} - n_{air}}. \tag{3.10}$$

3.2.2. Autocorrelator

To measure sample thickness with an autocorrelator, one of the beams needs to travel through the sample. The other one is guided over the delay, and the two beams then get focused into the BBO. A photodetector measures the intensity of the SHG from the overlap. Another photodetector takes a leakage measurement of the sample ray, which can be used for further improvement of the recorded data or to investigate changes in the sample. The delay line is placed on a motorized translation stage. The smallest achievable incremental movement of the servo motor is $50nm$, but typically, a step size of $300nm$ was used. A schematic of the autocorrelator used for this thesis can be seen in Figure 3.8.

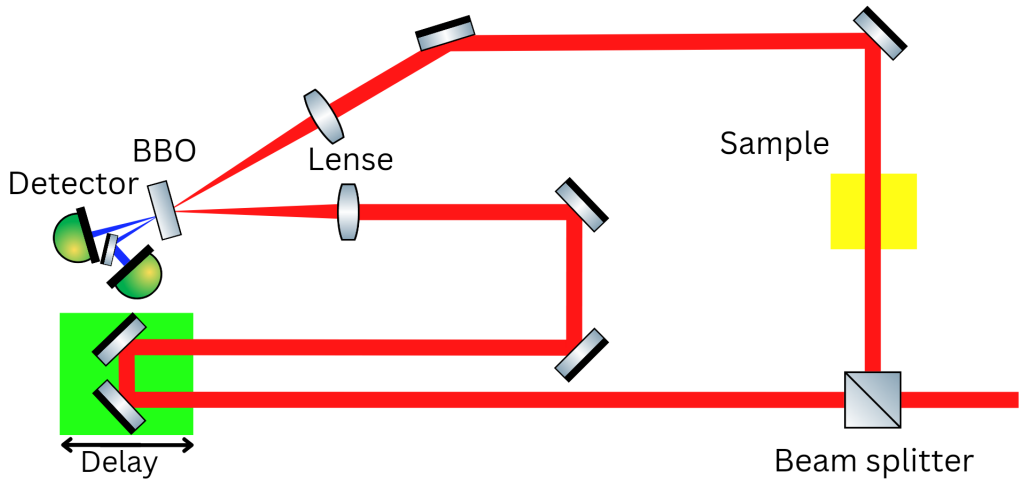

Figure 3.8.: Schematic of the intensity autocorrelator setup.

The autocorrelator built for this setup required high precision and repeatability. This means that the alignment is a crucial point which must be stable over the entire range of the delay line. Therefore a corner cube was used on the delay stage. A corner cube is an optical component consisting of three mirrors placed orthogonal to each other, as shown in Figure 3.9. An incoming beam of light gets reflected at least three times, on the orthogonal mirrors, in such a way that the outgoing beam is parallel to it. The two lenses are also used to improve precision. Because we do not want any interference

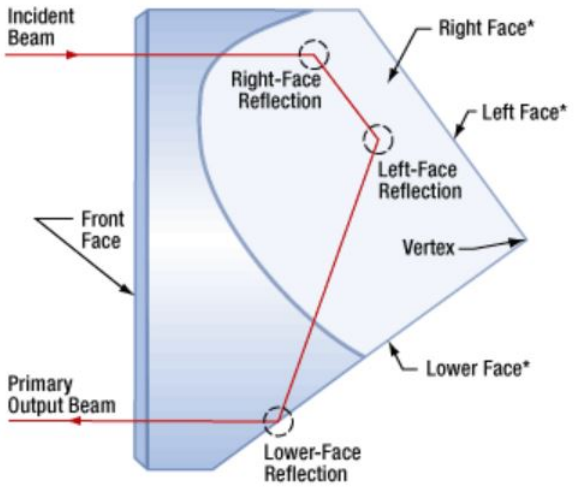

Figure 3.9.: Corner cube [11].

of the two light beams, it is impossible to build the setup in a collinear way. This means using only one lens to focus into the BBO crystal lead unavoidable to spherical aberrations, as shown in Figure 3.10. There are special lenses to avoid this effect, but

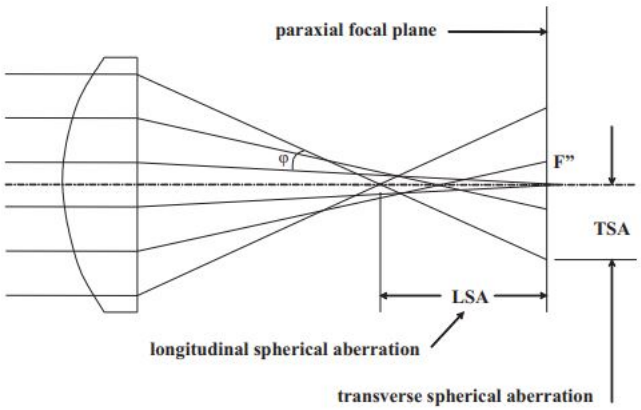

Figure 3.10.: Spherical aberration of a lens with F" being the focal point [3].

many of them have other disadvantages and are never perfect. The simplest solution is to hit the lens in the middle, this however requires two lenses in a non-collinear setup. As simple as this solution is in theory, the implementation of it depends on the two focal points overlapping in space as well as in time and still satisfying equation 3.4, imposing restrictions to the geometry and alignment. The final setup can be seen in Figure 3.11.

3.2.3. Measurement Software

To remotely control the acquisition of the thickness measurement LabVIEW program was written. On the front panel, as represented in Figure 3.12, the motor can be con-

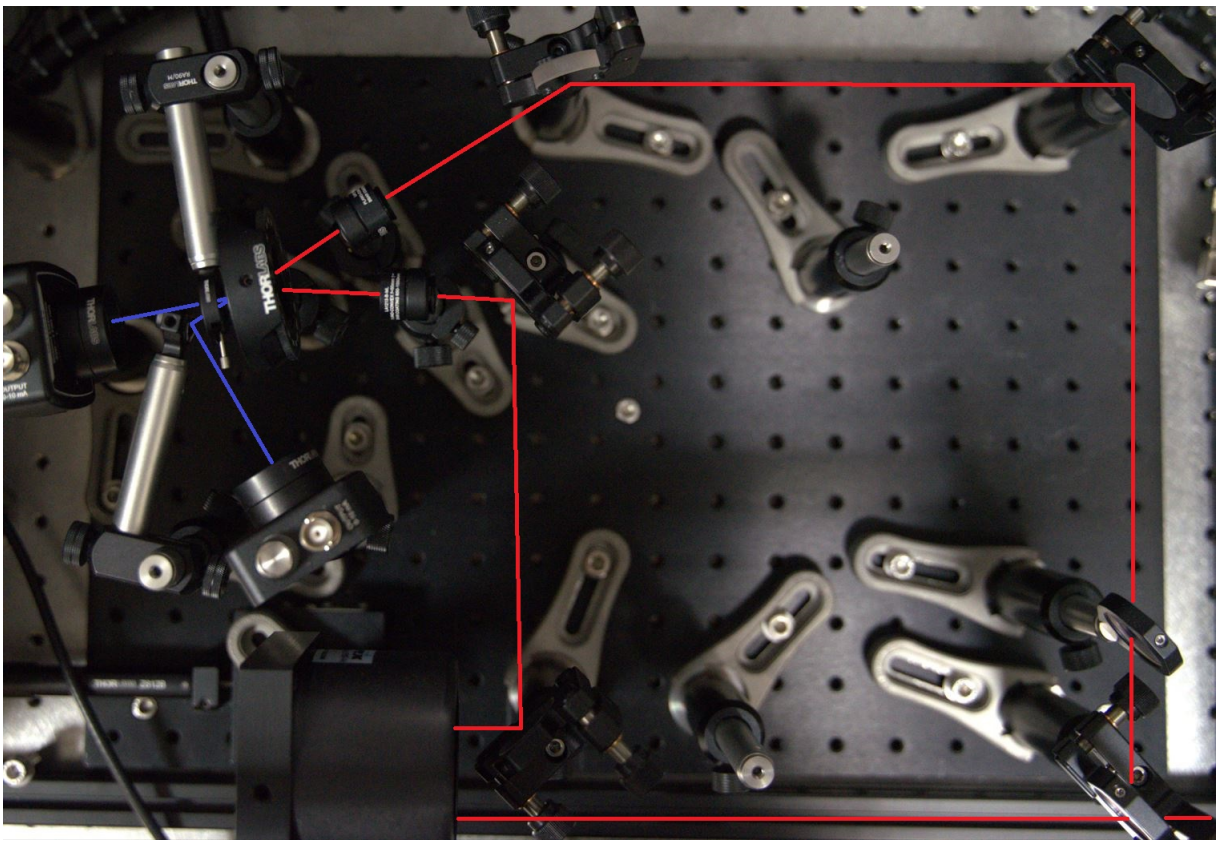

Figure 3.11.: Experimental setup of the intensity Autocorrelator.

trolled. Also, the starting position, end position, step size and the number of scans can be selected depending on the specific need. The Start button and Stop button start or stop the measurement. A panel determines the data file path. On the right-hand side at the top is a live voltage diagram of the overlap. On the bottom is a diagram of the last autocorrelation curve. After starting a measurement, the motor moves the delay stage to the starting position. A scan starts with a loop of 200 measurements of the voltage from both, the photo detector at the overlap and the photo detector at the leakage of the sample ray. The mean is calculated and stored with the position of the delay stage in an array. Now the servo motor moves with an increment of the step size. This process is repeated until the delay stage reaches the end position and a new scan starts. Each scan is then stored with date and time in an Excel file.

3.2.4. Operating the Autocorrelator

To ensure a stable Gaussian autocorrelation curve, an operating procedure should be followed when using the autocorrelator. First, turning on the laser is important, because this is a high-precision measurement, it is recommended to let the laser heat up for an hour. Otherwise, the data could be corrupted by fluctuations in pulse intensity. After that, the autocorrelation software can be started, and the first action is to home the

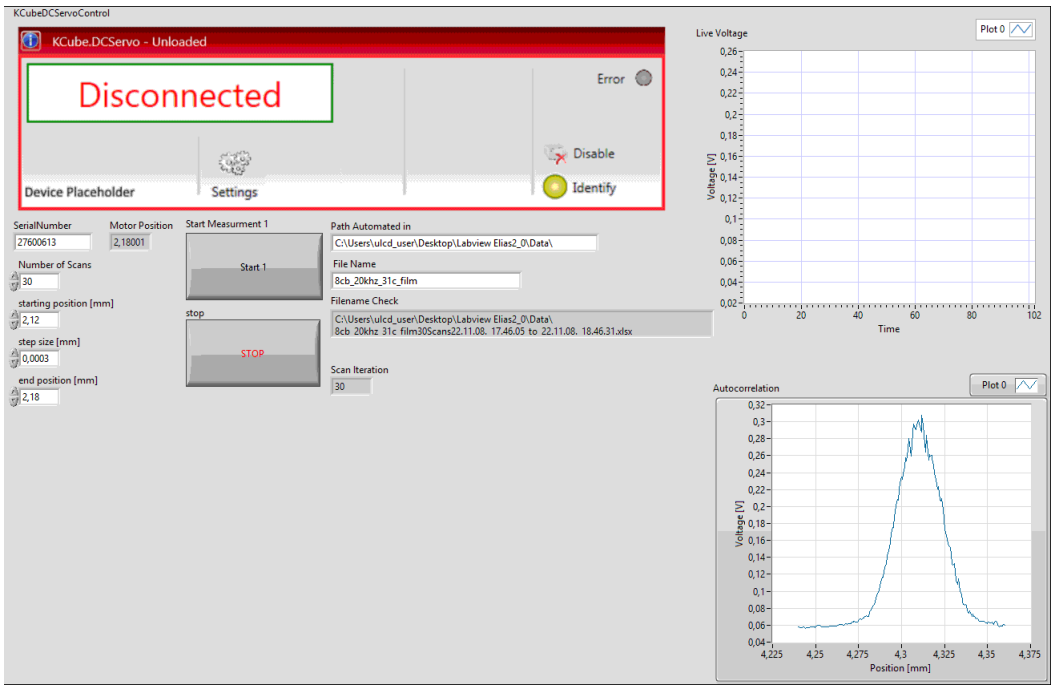

Figure 3.12.: LabVIEW autocorrelator frontpanel.

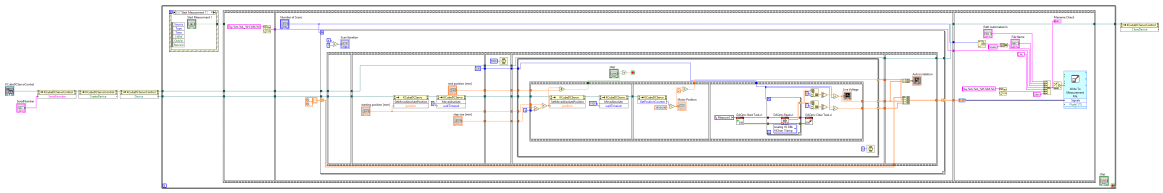

Figure 3.13.: LabVIEW autocorrelator block diagram.

servo motor by pressing the home button on the front panel. The peak position can fluctuate on a daily base, so conducting a first rough scan of the position where the peak is expected gives the exact range where to scan. Then the overlap needs to be optimized. This is done by moving the delay stage to the peak position and adjusting both mirrors right before the lenses until a maximum in intensity is reached. This process can change the delay position of the autocorrelation peak, therefore a second scan is recommended. In this second scan, there should now be a clean autocorrelation curve, as seen in Figure 3.7. If not, the overlap needs further improvement. With a clean Gaussian-shaped autocorrelation curve, the measurement can now be started with a reference measurement, followed by any number of sample measurements. When the shape deteriorates, another overlap adjustment can be performed. Note that moving the mirrors alters the optical path length, so the reference position is not accurate anymore.

4. Methods

4.1. Calibration Measurement

To check the accuracy of the setup, a calibration measurement with fused silica was conducted. A thin sheet of fused silica with a thickness of around $s_{silica} \approx 0.5mm$ was mounted in a rotational stage and measured for an angle of incidence from 90° to 95°. Each measurement included 10 scans, and a reference measurement was performed before and after. Due to refraction, the thickness of the tilted fused silica wafer is not the cosine projection of the thickness, as shown in Figure 4.1.

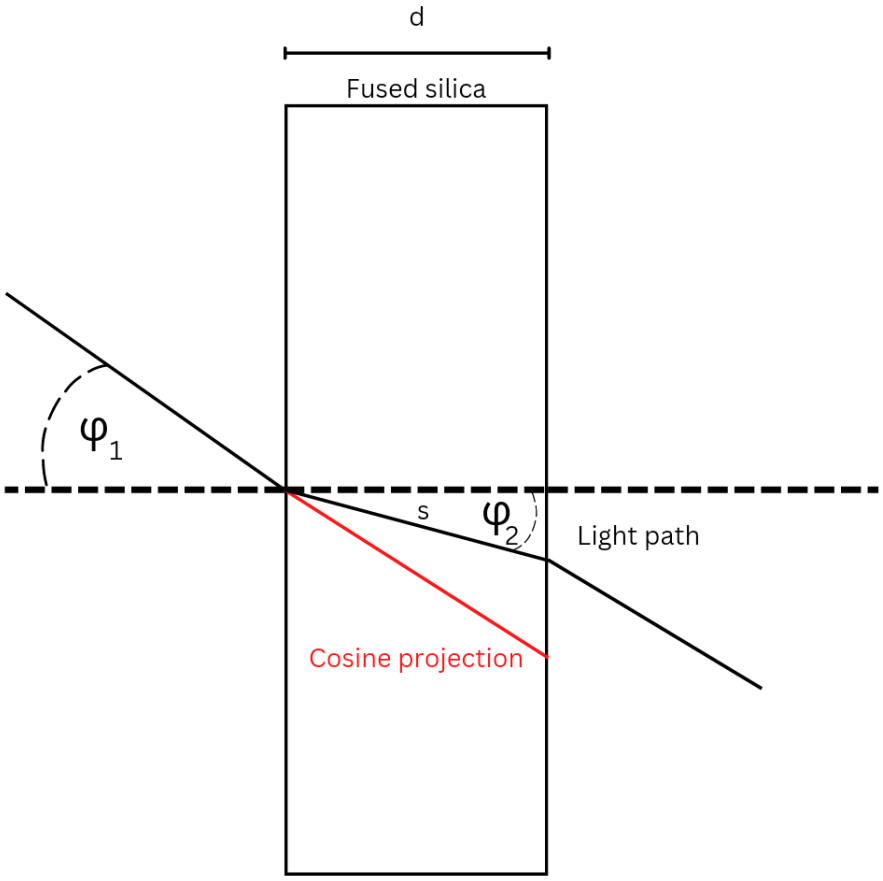

Figure 4.1.: Light path through the fused silica sample with an angle of incidence ϕ_1 and resulting angle ϕ_2, with a sample thickness of d and pathway s.

According to Snell's law, the theoretical optical path length through the fused silica

wafer, depending on the angle of incidence ϕ_1 can be calculated as

$$n_{fs}s = \frac{d}{\cos(\arcsin[\frac{\sin\phi_1}{n_{fs}}])}. \tag{4.1}$$

With $n_{fs} = 1.4533$ being the refractive index of fused silica [6]. Plotting the measured thickness and theoretical thickness over the angle of incidence, we obtain Figure 4.2. As sample thickness, the measured thickness at an angle of incidence of $0°C$ was used.

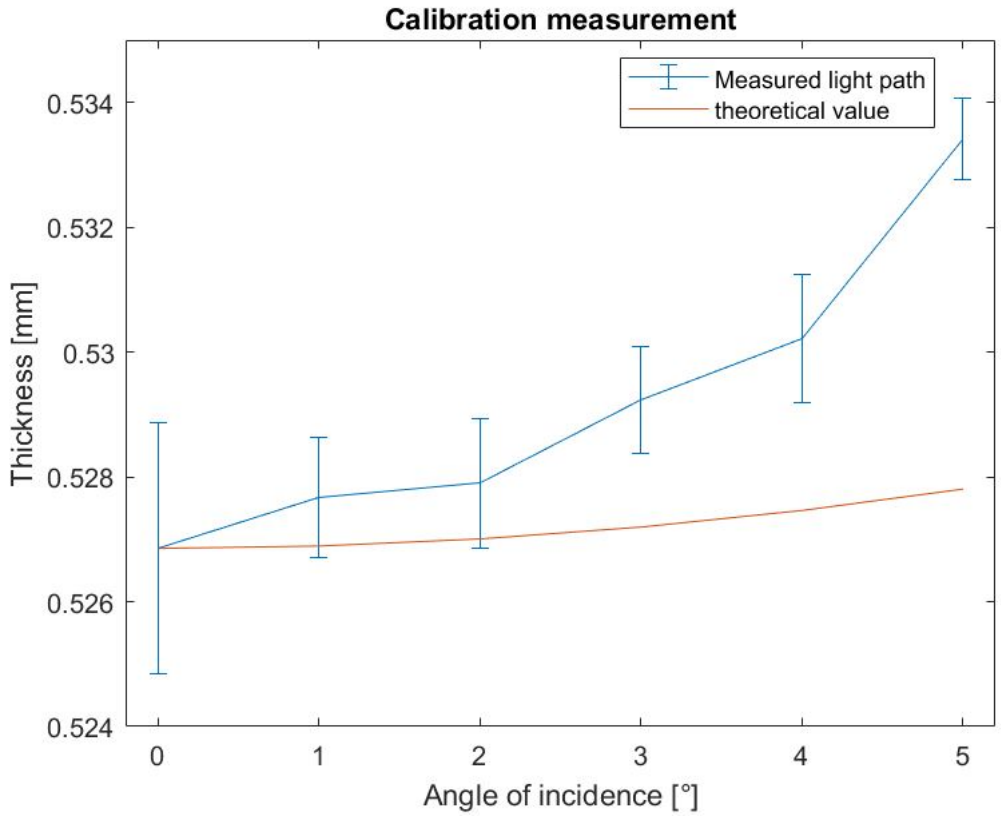

Figure 4.2.: Results of the calibration measurement. The length of the measured light path s and the theoretical length are plotted as a function of the angle of incidence. The thicknesses and errors are calculated as described in section 4.2.

There is a clear increasing of the light pathway as the angle of incidence deviates from the normal incidence. Equally visible is also the deviation from the expected values considering the fact that the fused silica substrate has a known thickness of 500 +- 25 micron. The explanation for this is the displacement of the light path in the plane of the fused silica wafer. A little difference in the exit point gets amplified by the reflection of the mirrors behind the sample, modulating the delay. Nonetheless, seeing only increasing thicknesses with the increasing angle of incidence, can give us an estimate of the accuracy. Comparing the points with the smallest theoretical increment at 0° and 1°, means we could distinguish a difference of about $40nm$.

4.2. Thickness Calculation

To extract the sample thickness from a set of measurements, some data analysis needs to be conducted. A set of measurements contains the reference measurement without the sample, this usually consist of ten scans. And a set of measurements with the sample. Here the number of autocorrelation curves that were recorded, is between 30 to 40 because we wanted to record the film behavior over the first hour after formation. For each of these autocorrelation curves, a Gaussian with offset was fitted to derive the peak position, see Figure 4.3.

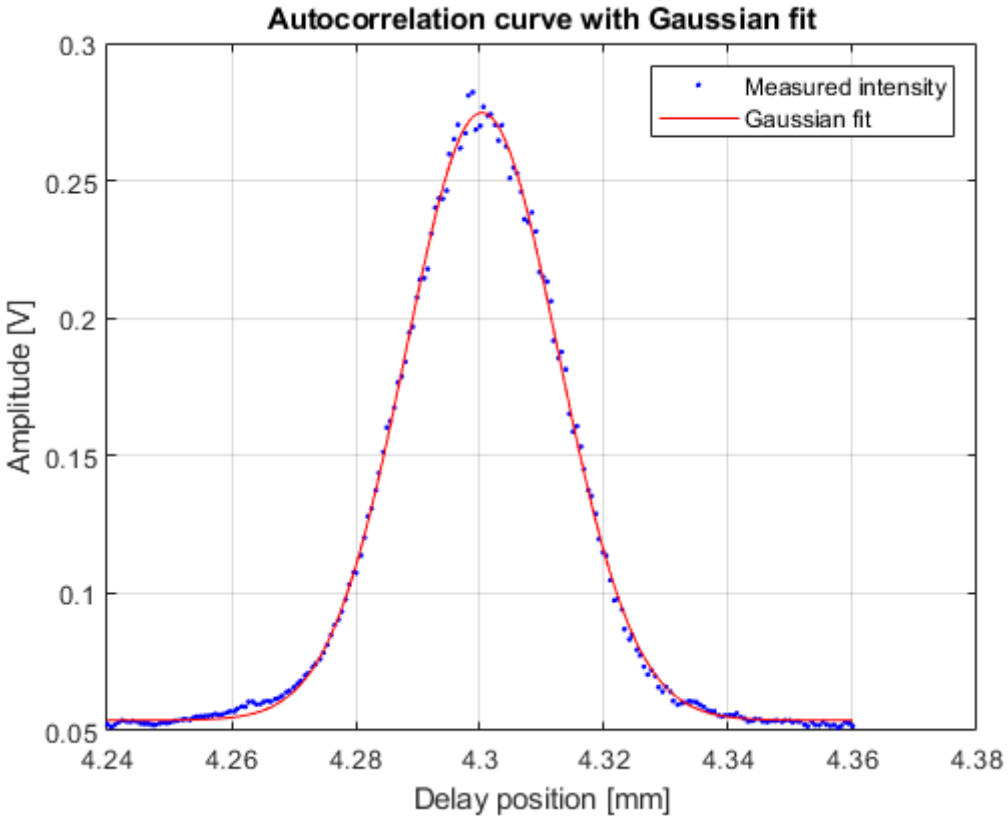

Figure 4.3.: Example of an autocorrelation curve with a Gaussian fit.

After deriving the peak position of all the autocorrelation curves in one set, the mean for the reference peak position and for the sample peak position was calculated. The error of the peak position was calculated from the standard deviation as

$$\Delta p = \sqrt{\frac{\frac{1}{N-1}\sum_{i=1}^{N}|p_i - p|^2}{N}}. \tag{4.2}$$

With N being the number of peaks used for calculating the mean, p_i the peak position of one scan and p the mean peak position. Having the sample peak position p_{sam} and the reference peak position p_{ref} the sample thickness can be calculated as follows

$$s_{sam} = \frac{p_{ref} - p_{sam}}{n_{sam} - n_{air}}. \tag{4.3}$$

With n_{sam} and $n_{air} \approx 1$ being the refractive index of the sample and air, respectively. The error on the thickness value can be obtained as

$$\Delta s_{sam} = \frac{\sqrt{\Delta p_{ref}^2 + \Delta p_{sam}^2}}{n_{sam} - n_{air}}. \tag{4.4}$$

The refractive index of 8CB is dependent on the temperature and the wavelength of incident light. There is no literature value in the temperature range from $20°C$ to $35°C$ at $800nm$ for this, so the refractive index of 8CB n_{8CB} was estimated from the works of ShinTson Wu et al. [10] on 5CB and I. Chirtoc et al. [4] on 8CB at $589nm$.

4.3. Film Relaxation Period

In the process of this thesis, a phenomenon of film relaxation was discovered. The free-standing LC films need a certain time to align in a stable manner after formation. The effect impacts in a clear way the autocorrelation measurements, as can be observed in Figure 4.4.

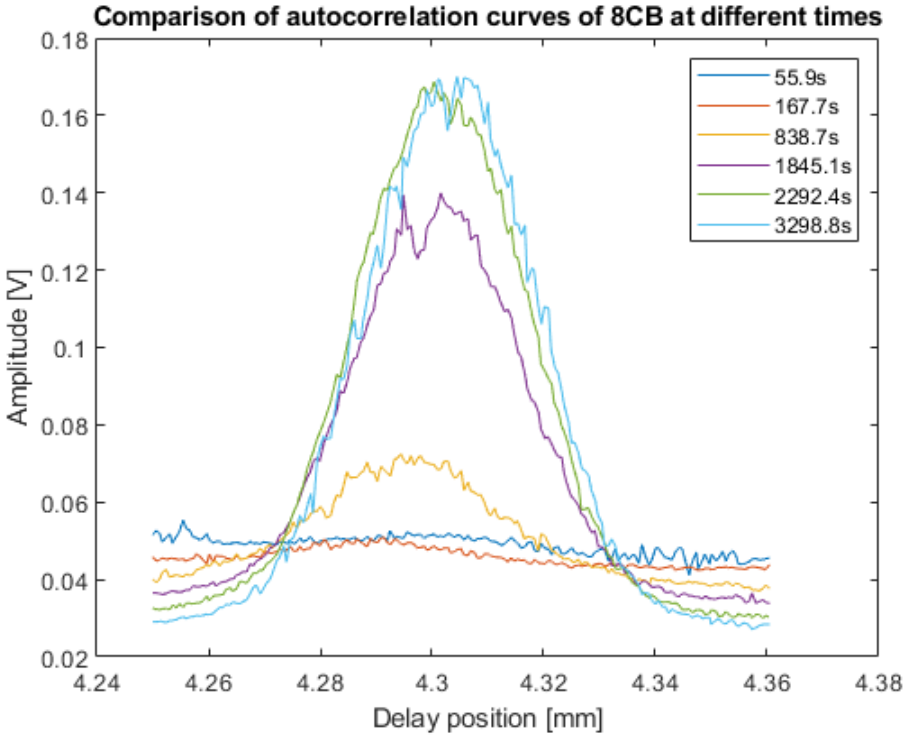

Figure 4.4.: Comparison of different autocorrelation curves, at different time intervals of a 8CB LC free-standing film, at $26°C$.

This effect is caused by the rearranging of the mesogens into a homeotropic surface from an initial somehow random configuration. The difference in peak intensity stems from the birefringent nature of 8CB. As long as they are not aligned, the LCs change the polarization of the incident light. The SHG crystal is only phase-matched for the polarization of the beam without a sample, meaning we lose conversion efficiency. Therefore the intensity of the autocorrelation peak drops. The amount of time needed for the film to be completely aligned seems to be dependent on the temperature and the film thickness. To gain further insight, the amplitude of the autocorrelation peak was plotted over time, as represented in Figure 4.5. The errors are the confidence intervals of the fits.

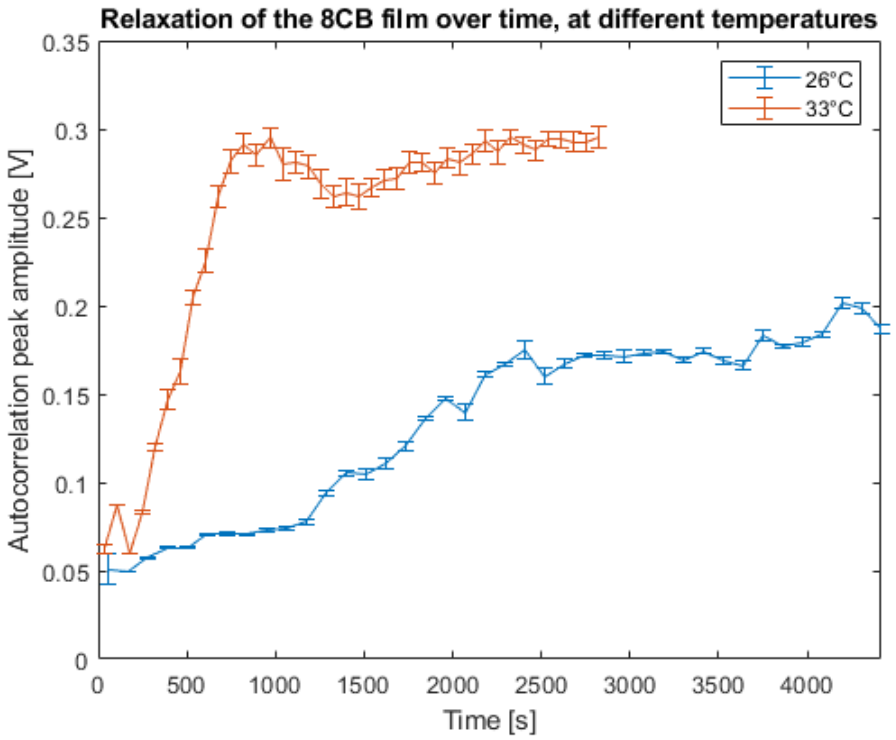

Figure 4.5.: Relaxation time of the free-standing 8CB film expressed as the autocorrelation peak intensity over time, for $26°C$ and $33°C$.

For higher temperatures, a dip can be seen right after the autocorrelation peak intensity reaches its maximum. There is currently no explanation for this phenomenon. The reason for that has to be searched probably in the LC orientation. A dedicated polarizing horizontal microscope is about to be built in order to have a clear evidence of the LC dynamics at hand. Nevertheless, it can be speculated that at higher temperatures, the molecules composing the LC film have more freedom to vibrate and move within the single layer surface. With the current time resolution of about one minute, it is possible that the drop off is caused by an average of said vibrations, this would be coherent with the multiple peaks present in some of the relaxation curves. A completely different behavior is observed at lower temperatures where a continuous modification of

the birefringence is observed. Extracting the LC film thicknesses while the film is not aligned is almost impossible because the Gaussian results with a different peak position because the optical path length is changed with the refractive index. Therefore only the peaks after the signal reaches the plateau were considered.

5. Results

5.1. LC Film Thickness

The thickness measurements were conducted for temperatures from $22°C$ to $35°C$ and wiper blade velocities from $2.5mm/s$ to $20mm/s$. In Figure 5.1, this is represented. It should be noted that for wiping speeds of $5mm/s$ and above, the LC films have the tendency to burst before the relaxation period was finished. Looking at the overall tendency, it appears that we have two different regimes. Below $26°C$, higher motor speeds result in thicker films, while above $33°C$ exactly the opposite is true. The in between temperatures, meaning $29°C$ and $31°C$, there is not a clear trend. In order to build a better understanding of the reason behind this behavior, we can look in detail for each motor speed at the time resolved temperature dependence.

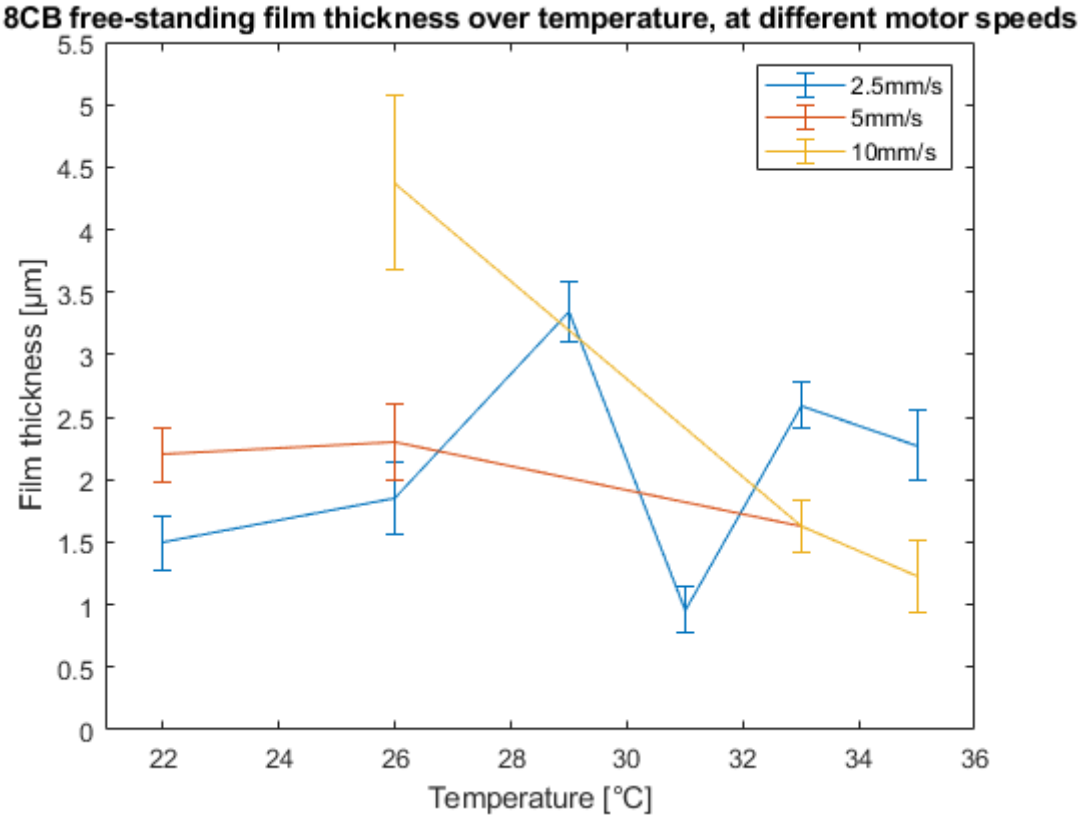

Figure 5.1.: Measured thickness of 8CB free-standing films for different wiper blade velocities and at different temperatures

5.2. Relaxation Period

In Figure 5.2 the autocorrelation peaks for different temperatures can be seen. The motor speed was fixed at $5mm/s$. Starting at $22°C$ and $26°C$ an almost continuous rising of intensity is displayed, until a small plateau, thus a stable alignment is achieved. This is opposite to the $35°C$ case, where the LC is expected to be nematic and a clear oscillatory behavior is observed. The in between temperatures show instead a critical behavior, similar to an inertial waiting time up to a certain threshold, after which a rearrangement is achieved independently by temperature, indicated by the similar slopes.

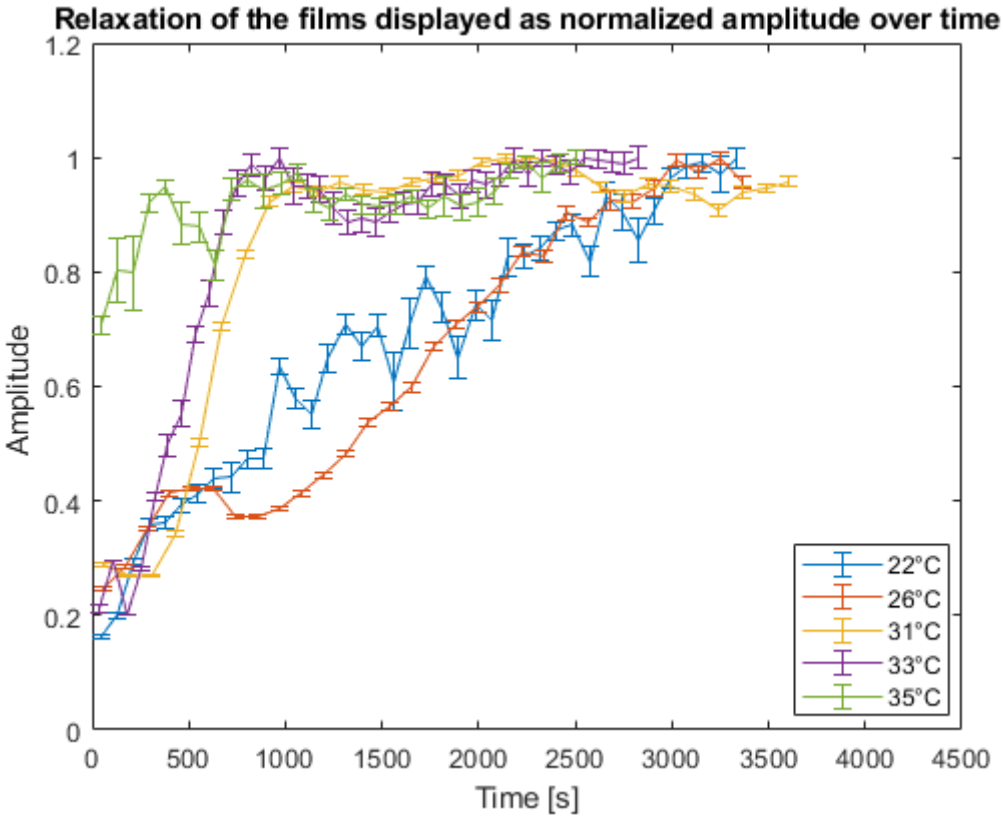

Figure 5.2.: Autocorrelation peak intensity at a wiping speed of $5mm/s$ over time, for different temperatures

Now for each temperature we look at different motor speeds. In Figure 5.3,at a temperature of $22°C$ the amplitude, of the measurement with a motor speed of $2.5mm/s$, rises steep, reaching a plateau after approximately $2000s$. In contrast to that, the measurement with a motor speed of $5.0mm/s$, has a slower rising time and behaves more like the measurements with a temperature of $26°C$ and $29°C$. The measurements conducted at $26°C$, look similar to each other, with a slow and steady rising slope, as represented in Figure 5.4. For the $31°C$ measurements, see Figure 5.5, this trend changes drastically, with a short and steep rising period followed by a plateau. The $33°C$ measurements (see

Figure 5.6) look similar to the previous ones, but with an even steeper slope and more fluctuations in the plateau. Here we can see a clear oscillation in the signal where the minimum is achieved at shorter time as faster the wiper motor goes, looking like as the wiping action can impart a faster alignment. In the last measurements at $35°C$ (see Figure 5.7), this trend continues. The plateau has even more fluctuations with a frequency modulation of $0.5mHz$ to $1.0mHZ$, as the motor speed goes from $2.5mm/s$ to $20mm/s$ (see 5.1). Here a rising slope can no longer be extracted since the oscillatory behavior dominates the curve profile, and the fact that the first rising of the signal happens in less than 2 minutes, shorted than the current time step resolution. The figures prove a strong correlation between the temperature and the time until the free-standing LC film is aligned. At closer consideration, a relation between wiping speed and relaxation time can be observed in Figures 5.4, 5.5 and 5.6. This being, a faster alignment with faster wiping speeds.
In an attempted to illustrate this better, the rising section of each measurement was fitted with a straight line and from that the slope was calculated, see Figure 5.8. As errors, the confidence intervals of the fits were used. The observations made before can be confirmed. Excepting the slope at $35°C$, because of time resolution of this measurement, the trend of, a steeper slope with rising temperature and wiping speed is visible.

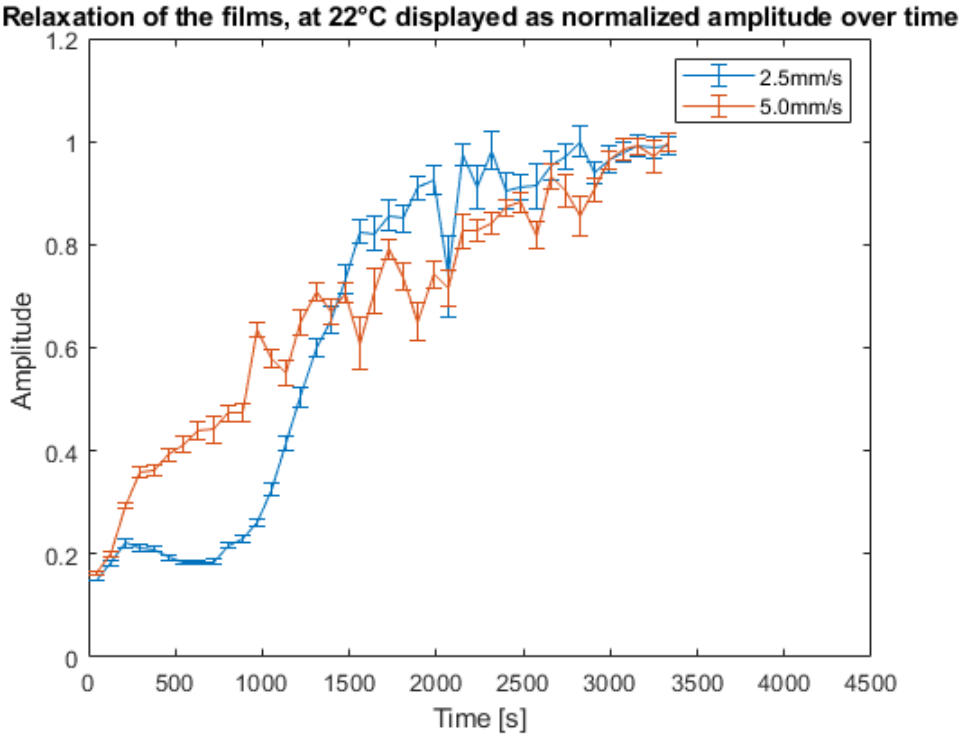

Figure 5.3.: Autocorrelation peak intensity at $22°C$ for different wiping velocities.

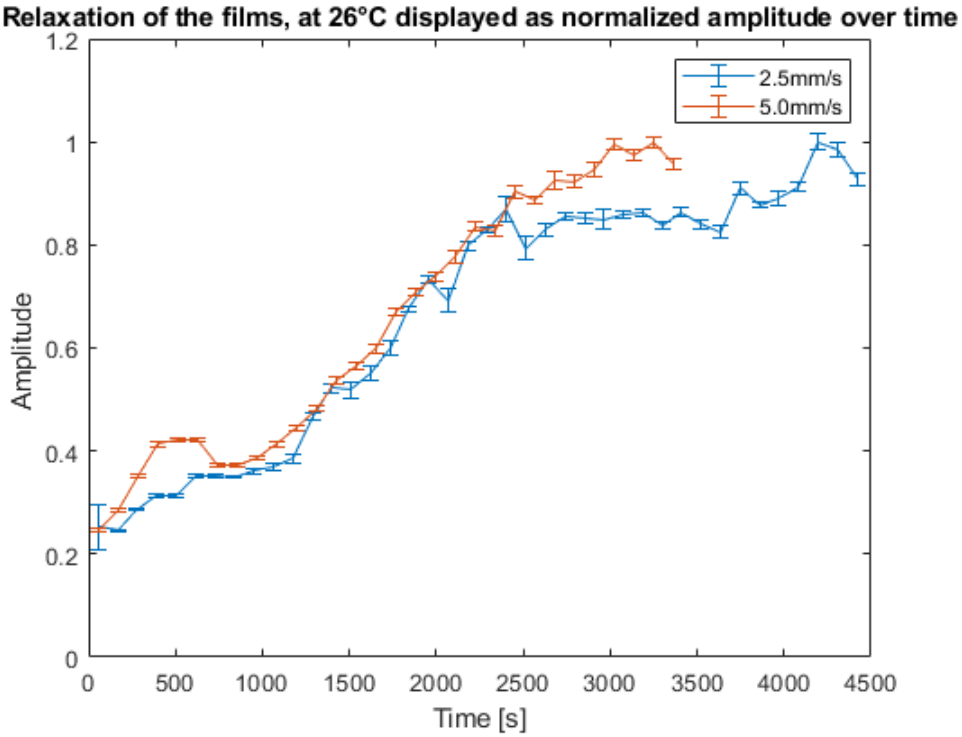

Figure 5.4.: Autocorrelation peak intensity at $26°C$ for different wiping velocities.

Motor speed [mm/s]	Frequency [mHz]	Frequency error [mHz]
2.5	0.549	0.053
5	0.733	0.288
10	0.820	0.192
20	0.991	2.36

Table 5.1.: The calculated frequencies and errors for the different motor speeds at $35°C$

For the measurements at $35°C$ an exponential rising sine was fitted (see Figure 5.9), to extract the frequency modulations of the oscillating plateau. The frequencies and errors are displayed in Table 5.1. As errors the confidence intervals of the fits were used. A trend of a higher oscillation frequency with higher motor speed can be observed.

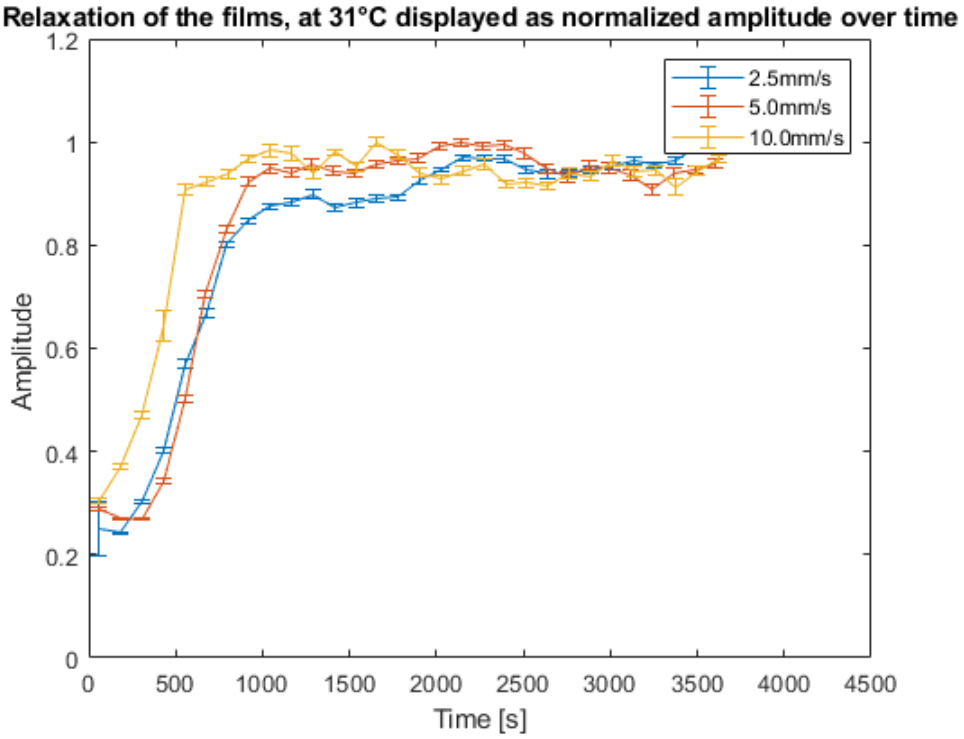

Figure 5.5.: Autocorrelation peak intensity at 31°C for different wiping velocities.

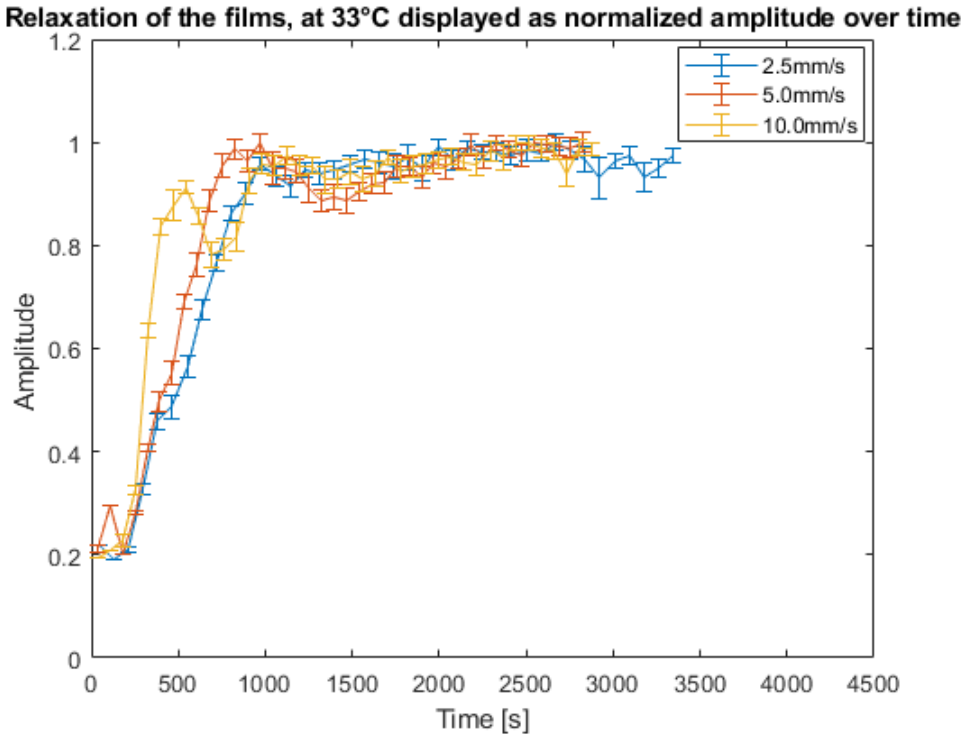

Figure 5.6.: Autocorrelation peak intensity at 33°C for different wiping velocities.

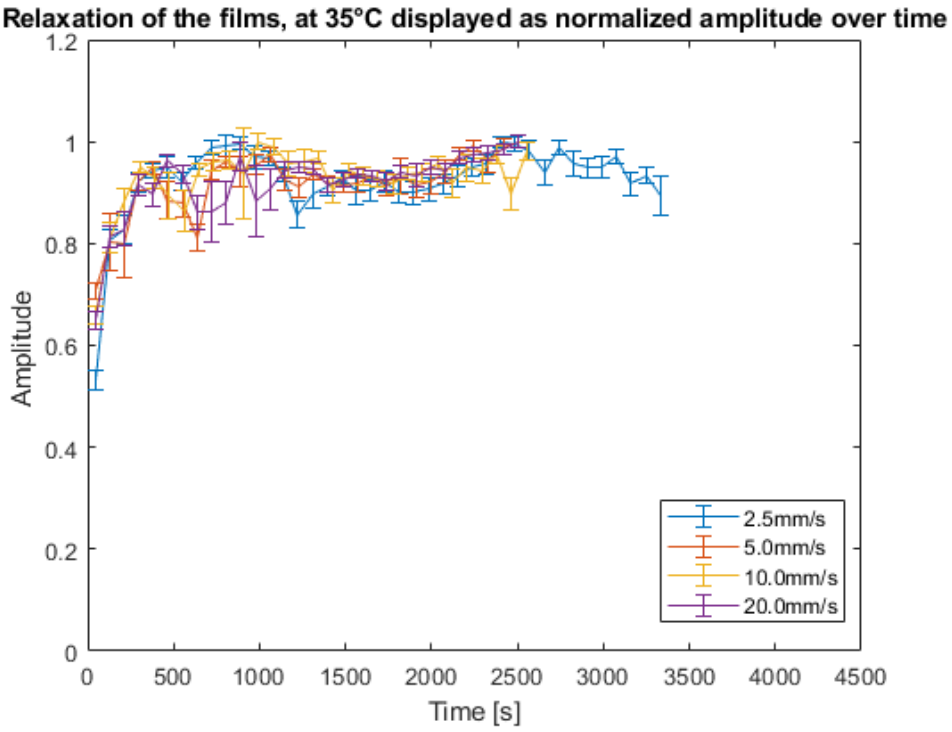

Figure 5.7.: Autocorrelation peak intensity at $35°C$ for different wiping velocities.

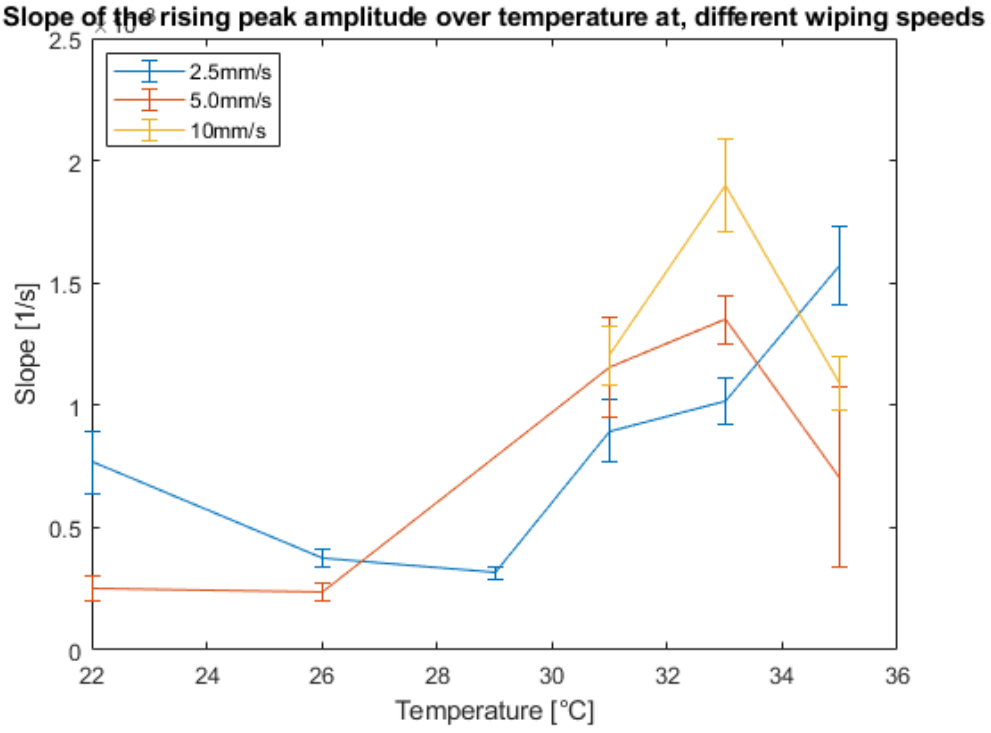

Figure 5.8.: Slope of the relaxation periods plotted over the temperature for different motor speeds.

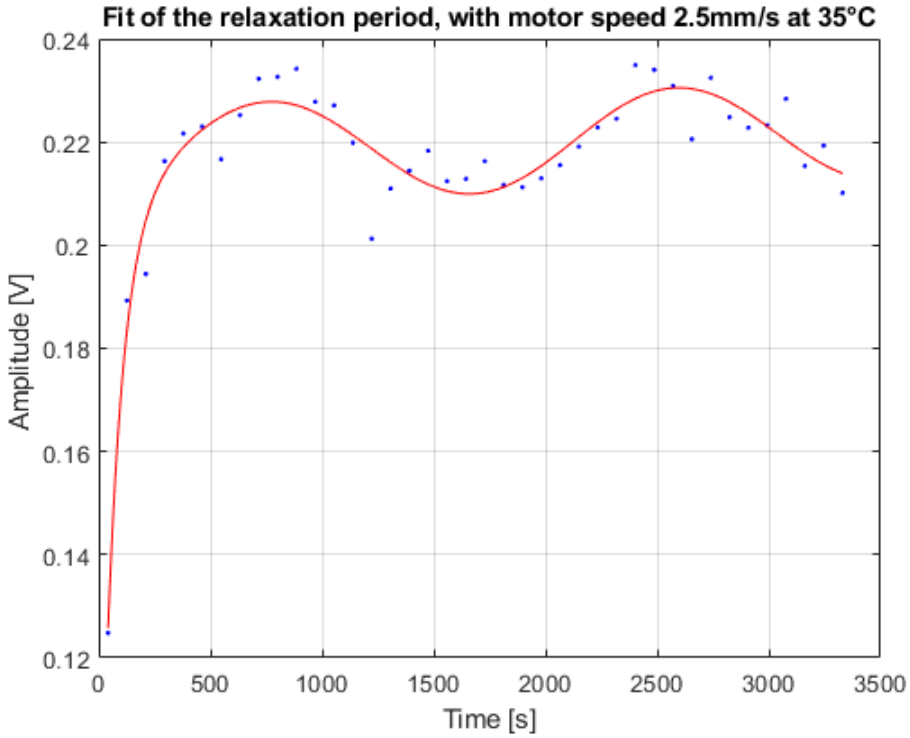

Figure 5.9.: Fit of the relaxation period at $35°C$ and a wiping speed of $2.5mm/s$.

6. Conclusions and Outlook

In this thesis, a detailed investigation of the thicknesses of formed free-standing 8CB films was performed as a function of LC temperature and wiping speed. The thickness measurement required the installation of an autocorrelator setup where a resolution of $\approx 0.2\mu m$ was achieved.
In the 18 thickness measurements that were carried out for this thesis, it was not possible to find a clear relation between the blade velocity and the film thickness, on the contrary, temperature seems to dominate the overall film formation and relaxation to a stable thickness. Comparing this to the thickness measurements conducted by Patrick L. Poole [8], it is essential to note that a clear dependency could only be found at wiping speeds of around $500\mu m/s$. The slowest speed used in this experiment was five times higher, this might explain the absence of a correlation. In order to have a clear idea of when the motor speed starts to impact on the film thickness, further investigations must be conducted to increase the statistical ensemble of cases, especially at speeds below $1mm/s$.
Another important factor that needs to be mentioned is the refractive index of 8CB. There is no literature concerning the temperature range and wavelength used in this setup, and the refractive index used was approximated by comparing the refractive index of 5CB at this temperature range and wavelength from the works of ShinTson Wu et al. [10] with the refractive index of 8CB at $589nm$ from the works of I. Chirtoc et al. [4]. To improve the accuracy of these measurements, an almost exact refractive index should be acquired.
Regarding the device to form the free-standing films, further improvements can be considered. First, the dispenser is too far from the actual position where the film is formed. Over that distance to the dispenser-hole, the LC can be distributed in a various ways, such that it is impossible to know the amount of LC around the sample hole. Moving the dispenser down right above the sample hole could improve this issue. Second, while testing the different blades, the importance of the contact pressure of the blade against the copper block became obvious. Being the most significant contributor to successful film formation, a thickness dependency is probable. A torque wrench, to measure contact pressure, or a clip-in mechanism that applies a variable amount of force could be used to investigate a possible correlation.
The film relaxation period is an interesting area of investigation, as it has hardly been researched so far. The relation between faster wiping speed and the faster relaxation of the free-standing LC films could be explained in terms of actual LC film thickness. Thicker films contain a larger bulk/surface ratio which means that, since air is the only factor imposing the homeotropic alignment of the entire free-standing film, the bigger the bulk is compared to the surface, the longer it will take the film to get aligned in

a stable manner. However, regarding the thickness measurement in Figure 5.1 this is not supported, because there is no visible correlation between motor speed and LC film thickness. An updated dispenser would prove useful for this as well.
Concerning the dynamical behaviour at higher temperatures, especially where oscillations appear at $33°C$ and $35°C$, a better time resolution is certainly needed to have precise results. To achieve that, the measurement could be performed with a reduction of the delay range. Albeit the full Gaussian curve would not be visible anymore, finding the peak intensity should still be possible and improving the time resolution by a factor of three. Another approach would be, to increase step size and reduce the number of photo detector events, exchanging the accuracy of the intensity for a better time resolution. With this method, the time resolution can be increased to a matter of seconds.
An investigation of the change in polarization should bring more clarity to the cause of the drop-offs. For this reason, a time-resolved imaging in crossed polarization is planned. Another measure to isolate this effect can be done by conducting the thickness measurement on free-standing LC films in the isotropic and crystalline phase.

List of Figures

List of Tables

Bibliography

[1] Liquid crystals in micron-scale droplets, shells and fibers. *J. Phys.: Condens. Matter*, 29(133003), 2017.

[2] Crystalline-like ordering of 8cb liquid crystals revealed by time-domain brillouin scattering. *Journal of Chemical Physics*, 151(014202), 2020.

[3] Svitlana Bielykh, Svitlana Subota, Victor Reshetnyak, and Tigran Galstian. Electro-optical characteristics of a liquid crystal lens with polymer network. *Ukrainian Journal of Physics*, 55:293–8, 01 2010.

[4] C. Glorieux Corresponding author J. Thoen I. Chirtoc, M. Chirtoc. Determination of the order parameter and its critical exponent for ncb (n=5–8) liquid crystals from refractive index data. *Liquid Crystals*, 31:2:229–240, 2004.

[5] Satyendra Kumar. *Liquid Crystal Experimental Study of Physical Properties and Phase Transitions*. Cambridge University Press, 2001.

[6] I. H. Malitson. Interspecimen comparison of the refractive index of fused silica. *J. Opt. Soc. Am.*, 55:1205–1208, 1955.

[7] Swamp Optics. Autococorrelation. *https://www.swampoptics.com/autocorrelation.html*.

[8] Patrick L. Poole. *Liquid Crystals as High Repetition Rate Targets for Ultra Intense Laser Systems*. PhD thesis, The Ohio State University, Columbus, Ohio, 2015.

[9] M Raghu Ramaiah, Avnish Sharma, Prasad Naik, P. Gupta, and Rashid Ganeev. A second-order autocorrelator for single-shot measurement of femtosecond laser pulse durations. *Sadhana*, 26:603–611, 12 2001.

[10] Marc Warenghem Mimoun Ismaili ShinTson Wu, Chiung-Sheng Wu. Refractive index dispersions of liquid crystals. *Optical Engineering*, 32(8):1775—1780, 08 1993.

[11] Thorlabs. Corner cube. *https://www.thorlabs.de/newgrouppage9.cfm?objectgroup$_i$d* = 145.

[12] Dario Polli V.P. Gupta Vikas Kumar, Nicola Coluccelli. *Molecular and Laser Spectroscopy*, chapter 5. Elsevier, 2018.

[13] Dmitry Yakovlev, V.G. Chigrinov, and H. Kwok. Chapter 1 of "modeling and optimization of lcd optical performance" (a sample chapter). 04 2015.

A. Appendix

Delay1 [mm]	Overlap1 [V]	Leak1 [V]	Delay2 [mm]	Overlap2 [V]	Leak2 [V]
4.240028	0.078938	0.055628	4.240028	0.053463	0.068156
4.240665	0.007081	0.005228	4.240607	0.053354	0.069106
4.241128	0.080733	0.053474	4.241244	0.054015	0.068514
4.241822	0.061603	0.038019	4.241764	0.053883	0.068345
4.242401	0.075177	0.057404	4.242459	0.053743	0.068123
4.24298	0.077289	0.0563	4.242922	0.053645	0.06772
4.243674	0.082071	0.057101	4.243732	0.053833	0.06857
4.24408	0.079831	0.056293	4.244022	0.05374	0.068622
4.244832	0.079458	0.058043	4.244832	0.054187	0.068591
4.245353	0.078217	0.056799	4.245353	0.054778	0.069232
4.246047	0.076108	0.056754	4.246047	0.05524	0.0697
4.246568	0.077682	0.057404	4.246568	0.055081	0.069383
4.247263	0.077608	0.057766	4.247263	0.054788	0.069386
4.247726	0.075605	0.057499	4.247668	0.054289	0.069227
4.24842	0.076327	0.057172	4.248478	0.053452	0.069003
4.248999	0.077201	0.05676	4.248941	0.05365	0.069159
4.249636	0.078052	0.057853	4.249636	0.054453	0.068023
4.250157	0.075628	0.058397	4.250099	0.053487	0.068511
4.250794	0.075805	0.058552	4.250851	0.053923	0.06859
4.251372	0.075251	0.058893	4.251314	0.054081	0.068886
4.252009	0.074792	0.058795	4.252067	0.054049	0.068934
4.252646	0.074243	0.058211	4.25253	0.055425	0.069132
4.253167	0.073926	0.05871	4.253224	0.056332	0.068884
4.253861	0.073886	0.059226	4.253861	0.056865	0.069924
4.254324	0.072031	0.059492	4.254324	0.056731	0.070613
4.255019	0.071726	0.059133	4.255077	0.056527	0.070003
4.255655	0.072109	0.059869	4.255597	0.055359	0.068776
4.25606	0.070782	0.060321	4.256118	0.054761	0.068493
4.256871	0.072151	0.059526	4.256813	0.055508	0.068998
4.257334	0.069805	0.060506	4.257392	0.055606	0.069948
4.258028	0.071204	0.058591	4.258028	0.054798	0.069266
4.258665	0.070127	0.060387	4.258665	0.054398	0.068784
4.259128	0.07009	0.060027	4.259128	0.055124	0.069187
4.259823	0.073189	0.056868	4.25988	0.055029	0.068623
4.260401	0.077426	0.060025	4.260344	0.054833	0.068346
4.26098	0.071561	0.061466	4.261038	0.05502	0.069066
4.261617	0.072239	0.060703	4.261559	0.05544	0.069121
4.262254	0.071347	0.061306	4.262254	0.056333	0.069918
4.262717	0.069208	0.061332	4.262774	0.056036	0.070087
4.263469	0.068945	0.060854	4.263353	0.056016	0.06905
4.26399	0.070055	0.060295	4.264048	0.055912	0.068913
4.264627	0.070843	0.061215	4.264511	0.056208	0.068976

Delay1 [mm]	Overlap1 [V]	Leak1 [V]	Delay2 [mm]	Overlap2 [V]	Leak2 [V]
4.265205	0.070273	0.061754	4.265263	0.056469	0.069188
4.265784	0.070945	0.06135	4.265726	0.056511	0.069105
4.266421	0.070529	0.060894	4.266479	0.057539	0.068979
4.267057	0.069518	0.061752	4.266942	0.058436	0.068617
4.26752	0.070159	0.061413	4.267578	0.057844	0.068902
4.268215	0.069885	0.062232	4.268215	0.055372	0.068332
4.268852	0.069159	0.062361	4.268852	0.055809	0.068232
4.269257	0.068327	0.062145	4.269257	0.056366	0.068963
4.270009	0.068652	0.062443	4.270009	0.05689	0.068372
4.270646	0.069266	0.062715	4.270646	0.056044	0.068031
4.271167	0.069826	0.062984	4.271167	0.056649	0.067746
4.271861	0.069179	0.061958	4.271861	0.056649	0.067271
4.272324	0.068409	0.06285	4.272382	0.056589	0.067667
4.273077	0.067904	0.06348	4.272961	0.057494	0.068226
4.273482	0.067495	0.063509	4.273598	0.057821	0.067443
4.274234	0.067746	0.063657	4.274177	0.057468	0.067005
4.274755	0.066461	0.062921	4.274813	0.057097	0.068198
4.27545	0.06658	0.063341	4.27545	0.058157	0.068469
4.275971	0.066278	0.063866	4.275913	0.058958	0.068636
4.276665	0.067173	0.064022	4.276665	0.059719	0.067311
4.277128	0.06569	0.06398	4.277128	0.059692	0.069541
4.277939	0.067189	0.064578	4.277939	0.060138	0.069433
4.278228	0.066054	0.064687	4.278228	0.060188	0.069108
4.279038	0.067046	0.064554	4.27898	0.05974	0.068569
4.279617	0.066894	0.065016	4.279675	0.059932	0.068406
4.280138	0.065558	0.06497	4.28008	0.060337	0.067736
4.280833	0.066637	0.064433	4.280833	0.060563	0.068107
4.281354	0.066799	0.064583	4.281411	0.061311	0.067979
4.28199	0.066624	0.063847	4.281932	0.061516	0.068432
4.282627	0.065893	0.064618	4.282627	0.061562	0.068718
4.283206	0.065959	0.065357	4.283206	0.061693	0.068792
4.283784	0.065895	0.065368	4.283842	0.062836	0.068509
4.284479	0.066611	0.06559	4.284421	0.063357	0.0683
4.284942	0.065956	0.065444	4.285	0.0632	0.068551
4.285637	0.064916	0.06503	4.285579	0.063517	0.068247
4.286157	0.065994	0.065193	4.286215	0.064731	0.06819
4.286852	0.066896	0.065677	4.286794	0.065785	0.067841
4.287373	0.06672	0.066102	4.287431	0.066051	0.067118
4.28801	0.065829	0.065647	4.287952	0.064988	0.066984
4.288588	0.065462	0.065518	4.288646	0.065924	0.068483
4.289225	0.067255	0.065861	4.289167	0.06711	0.068749
4.289862	0.067926	0.065688	4.289862	0.068684	0.068726
4.290383	0.066505	0.066067	4.290325	0.067899	0.068944
4.290961	0.066266	0.065869	4.291019	0.068147	0.067804
4.291656	0.06621	0.065854	4.291656	0.067707	0.068089

Delay1 [mm]	Overlap1 [V]	Leak1 [V]	Delay2 [mm]	Overlap2 [V]	Leak2 [V]
4.292119	0.067099	0.065631	4.292061	0.069747	0.068656
4.292814	0.066869	0.06564	4.292871	0.069903	0.06853
4.293392	0.066002	0.06594	4.293334	0.069047	0.069015
4.294029	0.065717	0.065556	4.294087	0.069122	0.068532
4.294666	0.066044	0.06547	4.294608	0.070964	0.068952
4.295129	0.06631	0.065495	4.295187	0.072368	0.068559
4.295823	0.066373	0.066012	4.295823	0.070755	0.069784
4.29646	0.066294	0.066299	4.29646	0.070568	0.06967
4.296865	0.066321	0.066403	4.296865	0.069158	0.069889
4.297675	0.065915	0.066558	4.297617	0.068353	0.069828
4.298138	0.066017	0.066737	4.298196	0.068472	0.070475
4.298775	0.065651	0.066883	4.298833	0.068845	0.070079
4.299354	0.065392	0.067303	4.299296	0.069737	0.069697
4.300048	0.065423	0.06724	4.300048	0.069897	0.069485
4.300511	0.066014	0.067213	4.300511	0.070491	0.069684
4.301264	0.066072	0.067427	4.301264	0.069052	0.069678
4.301727	0.065389	0.067673	4.301669	0.069968	0.069343
4.302479	0.065241	0.067393	4.302479	0.069902	0.069224
4.303	0.06522	0.067329	4.303	0.071595	0.069512
4.303579	0.065647	0.067038	4.303521	0.069118	0.069299
4.304158	0.065083	0.067418	4.304274	0.067561	0.069118
4.304794	0.064985	0.06749	4.304737	0.067664	0.069164
4.305373	0.065241	0.067773	4.305431	0.068255	0.068718
4.30601	0.065175	0.067934	4.305952	0.068715	0.06847
4.306647	0.064877	0.06811	4.306647	0.06923	0.067562
4.307167	0.064541	0.06783	4.307167	0.06729	0.067591
4.307804	0.064367	0.067783	4.307804	0.067833	0.06821
4.308383	0.064204	0.067989	4.308383	0.067625	0.068266
4.30902	0.063625	0.067767	4.30902	0.066484	0.068057
4.309598	0.063483	0.067418	4.309598	0.065988	0.068569
4.310177	0.063665	0.068023	4.310177	0.066455	0.06894
4.310814	0.063375	0.067735	4.310814	0.066115	0.068604
4.311451	0.063019	0.068012	4.311451	0.065297	0.068615
4.311856	0.063221	0.068008	4.311914	0.065336	0.06843
4.312666	0.063089	0.066815	4.312666	0.06499	0.068862
4.313187	0.062977	0.068541	4.313187	0.064145	0.068623
4.313766	0.063307	0.068248	4.313766	0.063625	0.068562
4.31446	0.062773	0.066804	4.31446	0.064087	0.06877
4.314923	0.062741	0.06754	4.314923	0.062847	0.068911
4.315676	0.061846	0.067448	4.315676	0.061958	0.069195
4.316139	0.061559	0.067459	4.316081	0.063035	0.069391
4.316833	0.061588	0.067912	4.316833	0.062462	0.068828
4.317412	0.06072	0.067339	4.317412	0.06027	0.069143
4.317933	0.060213	0.066851	4.317991	0.060493	0.068797
4.318685	0.059751	0.067707	4.318685	0.059622	0.067369

Delay1 [mm]	Overlap1 [V]	Leak1 [V]	Delay2 [mm]	Overlap2 [V]	Leak2 [V]
4.319091	0.060543	0.067817	4.319091	0.060339	0.066542
4.319843	0.060434	0.067727	4.319843	0.059907	0.066149
4.320306	0.058739	0.067321	4.320306	0.059423	0.066064
4.321001	0.058861	0.066883	4.321058	0.058626	0.066632
4.321579	0.060453	0.068382	4.321521	0.058927	0.067153
4.322216	0.059814	0.068738	4.322216	0.058249	0.066685
4.322795	0.058286	0.069438	4.322795	0.056491	0.066062
4.323374	0.058573	0.068308	4.323374	0.058504	0.06725
4.324068	0.058574	0.067598	4.324068	0.058648	0.066495
4.324473	0.058106	0.067767	4.324531	0.05601	0.068496
4.325284	0.058265	0.067543	4.325284	0.056459	0.068375
4.325747	0.056857	0.068065	4.325747	0.056351	0.067609
4.326383	0.056892	0.068364	4.326383	0.056633	0.066162
4.32702	0.058021	0.068021	4.32702	0.056865	0.066815
4.327599	0.056973	0.067917	4.327599	0.055781	0.067036
4.328235	0.056454	0.067991	4.328235	0.056235	0.067667
4.328698	0.057378	0.068686	4.328698	0.056013	0.068298
4.329451	0.05739	0.068651	4.329451	0.055662	0.067508
4.329972	0.056792	0.068514	4.329972	0.054888	0.067488
4.330608	0.056705	0.068778	4.330608	0.054738	0.06745
4.331187	0.056974	0.068538	4.331187	0.055194	0.067236
4.331824	0.057216	0.067746	4.331824	0.054976	0.067427
4.332461	0.05677	0.067797	4.332461	0.054448	0.067392
4.332866	0.057031	0.068596	4.332866	0.054865	0.066812
4.333676	0.057183	0.068924	4.333676	0.054621	0.065983
4.334139	0.057019	0.068746	4.334139	0.0542	0.066107
4.334776	0.056705	0.068952	4.334834	0.0545	0.068045
4.335412	0.056321	0.069172	4.335354	0.054904	0.067904
4.335991	0.055954	0.069253	4.336049	0.054435	0.067875
4.336628	0.056102	0.069126	4.33657	0.054648	0.067723
4.337264	0.054885	0.069625	4.337264	0.055268	0.067665
4.337727	0.055084	0.068723	4.33767	0.054691	0.06707
4.33848	0.056556	0.068179	4.33848	0.055029	0.066727
4.338943	0.056119	0.068903	4.338943	0.054753	0.067801
4.33958	0.05563	0.068723	4.33958	0.054448	0.06778
4.340216	0.05567	0.068759	4.340216	0.054596	0.067326
4.340795	0.054698	0.069016	4.340795	0.054445	0.067519
4.341374	0.053764	0.068535	4.341316	0.054208	0.068031
4.342011	0.054249	0.067369	4.342011	0.054506	0.068348
4.342647	0.055034	0.067741	4.342647	0.055005	0.068641
4.343168	0.054875	0.068736	4.34311	0.055488	0.069298
4.343863	0.055258	0.069039	4.343863	0.055746	0.068039
4.344326	0.055842	0.068947	4.344326	0.054493	0.065249
4.345078	0.055129	0.069433	4.34502	0.053822	0.06503
4.345483	0.054408	0.067907	4.345657	0.054233	0.066078

Delay1 [mm]	Overlap1 [V]	Leak1 [V]	Delay2 [mm]	Overlap2 [V]	Leak2 [V]
4.346236	0.054957	0.068511	4.346062	0.053498	0.066273
4.346757	0.05439	0.068847	4.346872	0.052835	0.066796
4.347451	0.054962	0.069423	4.347393	0.053605	0.066973
4.347856	0.054513	0.068976	4.347914	0.053989	0.06716
4.348667	0.056172	0.069581	4.348667	0.053956	0.067678
4.349187	0.056454	0.069465	4.34913	0.054215	0.067556
4.349824	0.055044	0.069066	4.349882	0.054582	0.068079
4.350345	0.055223	0.069481	4.350345	0.052291	0.068417
4.35104	0.055398	0.069992	4.35104	0.052278	0.066173
4.351561	0.055202	0.069245	4.351503	0.052875	0.066266
4.352197	0.054472	0.069383	4.352255	0.052315	0.066778
4.352776	0.054073	0.069261	4.352776	0.05264	0.065906
4.353413	0.053909	0.068338	4.353413	0.0528	0.066221
4.353991	0.054073	0.068635	4.353991	0.053181	0.066756
4.354628	0.054266	0.068565	4.354628	0.053196	0.066899
4.355207	0.055049	0.069037	4.355207	0.052231	0.066915
4.355786	0.05478	0.069298	4.355786	0.051897	0.067152
4.356422	0.054614	0.069448	4.356422	0.0525	0.067504
4.357059	0.054751	0.069383	4.357059	0.051592	0.067475
4.35758	0.054394	0.069419	4.35758	0.051749	0.067292
4.358217	0.055179	0.069362	4.358159	0.052958	0.067598
4.358738	0.054606	0.068981	4.358795	0.053344	0.067129
4.359432	0.054997	0.069317	4.359374	0.054363	0.067839
4.359895	0.054891	0.069782	4.360011	0.053851	0.067579

Table A.1.: Measurement file, of the first two scans, of the free-standing LC film thickness measurement, at a temperature of $31°C$ and a wiping speed of $2.5mm/s$. From this file the first to rows of the next table can be calculated.

Time [s]	Intensity [V]	$\Delta Intensity[V]$	Peak position [mm]
61.4	0.072444253	0.015489318	4.241175253
184.2	0.070133362	0.000448686	4.298921959
307	0.088009683	0.000959855	4.298430144
429.8	0.116767547	0.00148837	4.298484842
552.6	0.165261265	0.002591534	4.298208043
675.4	0.194128329	0.002435758	4.298156097
798.2	0.232771063	0.001749551	4.298580664
921	0.245929072	0.001748783	4.29928719
1043.8	0.254192665	0.001637171	4.299853706
1166.6	0.256674126	0.002105846	4.300135369
1289.4	0.260957701	0.002308298	4.300444413
1412.2	0.253305677	0.002178045	4.300562665
1535	0.256075581	0.00220757	4.300356946
1657.8	0.258539123	0.002515827	4.300587458
1780.6	0.259082367	0.001707573	4.300569349
1903.4	0.268274399	0.001971772	4.300745327
2026.2	0.274709646	0.00132239	4.300327974
2149	0.281537025	0.00164165	4.300272532
2271.8	0.281307479	0.001895307	4.300211351
2394.6	0.281139236	0.00183585	4.300499118
2517.4	0.274470453	0.002056427	4.300480859
2640.2	0.272290214	0.00222057	4.300725394
2763	0.272535336	0.002210767	4.300885605
2885.8	0.274559112	0.002219115	4.300837607
3008.6	0.276940937	0.002105422	4.300737837
3131.4	0.280216697	0.001942774	4.301287264
3254.2	0.277359411	0.001571692	4.30127224
3377	0.279884176	0.00157673	4.301401295
3499.8	0.288241999	0.001744075	4.301415186
3622.6	0.29035651	0.001462417	4.30134687

Table A.2.: Example of a result file. Time of the scan, the calculated peak intensity, the error of the calculated peak intensity and the calculated peak position, of the free-standing LC film thickness measurement, at a temperature of $31°C$ and a wiping speed of $2.5mm/s$.

Eidesstattliche Erklärung

Hiermit versichere ich, die vorliegende Arbeit selbstständig und unter ausschließlicher Verwendung der angegebenen Literatur und Hilfsmittel erstellt zu haben.
Die Arbeit wurde bisher in gleicher oder ähnlicher Form keiner anderen Prüfungsbehörde vorgelegt und auch nicht veröffentlicht.

Heidelberg, 23.11.2022

Elias Bürkle